
LEARNING DYNAMICAL SYSTEMS FROM INVARIANT MEASURES

Jonah Botvinick-Greenhouse*
Center for Applied Mathematics
Cornell University
Ithaca, NY 14850
jrb482@cornell.edu

Robert Martin
DEVCOM Army Research Laboratory
Research Triangle Park
Durham, NC 27709
robert.s.martin163.civ@army.mil

Yunan Yang
Institute for Theoretical Studies
ETH Zürich
Zürich, Switzerland 8092
yunan.yang@eth-its.ethz.ch

January 13, 2023

ABSTRACT

We extend the methodology in [65] to learn autonomous continuous-time dynamical systems from invariant measures. We assume that our data accurately describes the dynamics' asymptotic statistics but that the available time history of observations is insufficient for approximating the Lagrangian velocity. Therefore, invariant measures are treated as the inference data and velocity learning is reformulated as a data-fitting, PDE-constrained optimization problem in which the stationary distributional solution to the Fokker–Planck equation is used as a differentiable surrogate forward model. We consider velocity parameterizations based upon global polynomials, piecewise polynomials, and fully connected neural networks, as well as various objective functions to compare synthetic and reference invariant measures. We utilize the adjoint-state method together with the backpropagation technique to efficiently perform gradient-based parameter identification. Numerical results for the Van der Pol oscillator and Lorenz-63 system, together with real-world applications to Hall-effect thruster dynamics and temperature prediction, are presented to demonstrate the effectiveness of the proposed approach.

Keywords Dynamical systems · Invariant measure · Inverse Frobenius–Perron problem · Parameter identification · Fokker–Planck equation · Neural networks · Time-delay embedding · Computational ergodic theory

1 Introduction

Data-driven models have proven to be instrumental across numerous scientific disciplines for their ability to predict and control the behavior of complex physical systems [47]. The method by which models are constructed is highly dependent on the available data, as well as prior knowledge of the physical process in question. Popular approaches such as the shooting methods [2, 46], neural differential equations [8, 29, 49], and SINDy [6] adopt a *Lagrangian* perspective and seek to directly minimize the error between modeled trajectories and observed data. However, the following scenarios can render these standard techniques unreliable. *The observational data may be sparsely and irregularly sampled in time, such that derivatives cannot be accurately approximated. In a worst-case scenario, one may not even know the times at which individual samples were drawn. Moreover, measurements may be contaminated with large amounts of noise and the system in question could be highly sensitive to initial conditions.*

In the specialized setting of traffic simulation, the issue of sparse sampling was approached by merging the tasks of imitation learning, and interpolation under a single generative adversarial network [63]. Moreover, the Ensemble-SINDy method learns noisy chaotic dynamics by averaging over a family of models formed using bootstrapped samples [17]. However, a general modeling framework that is robust to each of the aforementioned difficulties remains elusive.

In [21, 65], an *Eulerian* perspective was adopted to handle such difficulties, and velocity models were constructed to yield the same asymptotic statistics as the observed measurements, rather than seeking a pointwise match with time

*Corresponding author

trajectories or Lagrangian velocities. More specifically, instead of directly treating the noisy observations $\{\mathbf{x}^\eta(t_i)\}_{i=1}^n$ of an autonomous flow $\dot{\mathbf{x}} = v^*(\mathbf{x})$ as inference data, the approaches in [21, 65] considered the *occupation measure* ρ^* , where for each measurable set B ,

$$\rho^*(B) := \frac{1}{n} \sum_{i=1}^n \chi_B(\mathbf{x}^\eta(t_i)), \quad \chi_B(x) = \begin{cases} 1, & x \in B, \\ 0, & x \notin B. \end{cases} \quad (1)$$

When the occupation measures generated by a set of initial conditions all weakly converge to the same *invariant measure* and the set of initial conditions has nonzero Lebesgue measure, such an invariant measure is said to be *physical* [66]. These convergence properties can be delicate, and an overview of the relevant theory is provided in Section 2.1. In this work, we consider the class of autonomous systems for which the occupation measures of almost all initial conditions converge to a unique physical measure. Notably, this encompasses chaotic attractors such as the Lorenz-63 system [39, 60].

Going forward, we write $v = v(\theta) = v(\mathbf{x}; \theta)$ to denote the dependence of the reconstructed velocity fields on a set of parameters $\theta \in \Theta$ where $\Theta \subset \mathbb{R}^m$ is the admissible set of all parameter values. The concrete form of θ depends on the hypothesis space of v , which will be discussed in Section 4.2. The task is now to find the best-parameterized model $v(\mathbf{x}; \theta)$ approximating the true velocity v^* by minimizing the mismatch

$$\inf_{\theta \in \Theta} \mathcal{J}(\theta), \quad \mathcal{J}(\theta) := \mathcal{D}(\rho_\varepsilon(v(\theta)), \rho^*). \quad (2)$$

The formulation (2) represents an inverse data-matching optimization problem, in which \mathcal{D} denotes a metric or divergence on the space of probability measures and $\rho_\varepsilon(v(\theta))$ is a regularized approximation to the physical measure of the dynamical system, given some regularization parameter $\varepsilon > 0$ and the current velocity $v(\theta)$.

Although one could approximate $\rho(v(\theta))$ by numerically integrating a trajectory and binning the observed states to a histogram [21], this approach does not permit simple differentiation of the resulting measure with respect to the parameters θ . When the size of θ is large, it is practical to use gradient-based optimization methods for solving the optimization problem (2), and one has to compute the essential gradient $\partial_\theta \mathcal{J}$. In [65], this was handled by viewing $\rho_\varepsilon(v(\theta))$ as the dominant eigenvector of a regularized Markov matrix originating from an upwind finite volume discretization of the continuity equation. The derivative $\partial_\theta \mathcal{J}$ was then seamlessly computed via the adjoint-state method [65]. The computation time of the adjoint-state method is independent of the size of θ , making the framework presented in [65] well-suited for large-scale computational inverse problems.

Different from [65], we consider the Fokker–Planck equation as the partial differential equation (PDE) forward model for $\rho_\varepsilon(v(\theta))$, rather than the continuity equation. This is motivated by the Fokker–Planck equation’s larger modeling capacity. Indeed, the Fokker–Planck equation reduces to the continuity equation when its diffusion term is zero, and it can fit intrinsic noise present in trajectories which reduces over-fitting the parameterized velocity $v(\theta)$. Moreover, the Fokker–Planck equation can be seen as an alternative to the teleportation regularization used for the continuity equation in [65], in order to guarantee the uniqueness of the computed stationary solution $\rho_\varepsilon(v(\theta))$.

In this work, we build upon the framework proposed in [65] and investigate dynamical system velocity learning with a *large-scale* parameter space applied to *real data*. There are three essential new contributions. First, we use an isotropic diffusion to regularize the forward continuity equation, which differs from the so-called teleportation technique [20] proposed in [65]. Second, in contrast to only learning three coefficients as done in [65], we parameterize the velocity $v(\theta)$ using piecewise polynomial, global polynomial, and neural network discretizations, which can all yield large parameter spaces with thousands of dimensions. We compare the reconstructed velocity in each case and further discuss how the choice of parameterization affects the inverse problem’s well-posedness and the reconstructed velocity’s regularity. We also consider various metrics/divergences as the choice of the objective function. Third, we investigate velocity learning in time-delay coordinates, which can characterize the full dynamics even with partial state measurements [59]. It is worth noting that there is no analytic form for the velocity in time-delay coordinates, even for well-studied dynamical systems. The proposed differentiable forward model and gradient-based methods are powerful and scalable tools for modeling time-delayed dynamics, and they permit larger-scale modeling than the approaches proposed in [21].

The paper is organized as follows. In Section 2, we review essential background on dynamical systems, invariant measures, the Fokker–Planck equation, and time-delay embedding. In Section 3, we introduce the forward surrogate model $\rho_\varepsilon(v(\theta))$ and analyze its modeling errors. In Section 4, we present an efficient gradient calculation for the objective function $\mathcal{J}(\theta)$ by treating (2) as a PDE-constrained optimization problem and utilizing the adjoint-state method. We then adapt the gradient calculation to various velocity parameterizations, including neural network discretizations in which the gradient is computed along with the backpropagation technique [35]. Finally, in Section 5, we present velocity reconstructions for the Van der Pol oscillator and the Lorenz-63 system. We also model dynamics in time-delay coordinates based on real-world data from a Hall-effect thruster, and we provide an example of temperature prediction with uncertainty quantification. Conclusions and further discussions follow in Section 6.

2 Background

This section reviews the essential background on invariant measures, stochastic dynamics, the Fokker–Planck equation, and time-delay coordinates. Finally, we review the Eulerian approach for parameter identification proposed in [21, 65], as well as prior work on the discrete inverse Frobenius–Perron problem [45].

2.1 Physical Measures and SRB Measures

Physical measures characterize the long-term statistical behavior of a physically significant subset of dynamical trajectories. When a dynamical system is chaotic and exhibits sensitive dependence on initial conditions, the existence of a physical measure unifies the statistical properties of trajectories which are pointwise dissimilar. While ergodic measures also describe the long-term statistical behavior of dynamical trajectories, they may have very small support or, in fact, be singular, which makes them difficult to observe computationally. On the other hand, if a dynamical system admits a physical measure, it holds that the dynamical trajectories corresponding to a positive Lebesgue measure subset of initial conditions will all share the same statistical behavior. We will next formalize these ideas using the language of ergodic theory. For a more thorough treatment of physical measures and the foundations of ergodic theory, the reader is encouraged to consult [9, 19, 66] and [14, 30, 43, 48], respectively.

Following [66], we assume that \mathcal{M} is a compact Riemannian manifold and that $T : \mathcal{M} \rightarrow \mathcal{M}$ is a diffeomorphism. A probability measure μ is said to be *invariant* with respect to the map T if $\mu(T^{-1}(B)) = \mu(B)$ for all $B \in \mathcal{B}$, where \mathcal{B} denotes the Borel σ -algebra [14, Definition 2.1]. Hereafter, we will assume that μ is an invariant measure. A point $x \in \mathcal{M}$ is said to be *generic* [66, Section 2.2] if for all $g \in C(\mathcal{M})$, it holds that

$$\lim_{N \rightarrow \infty} \frac{1}{N} \sum_{k=0}^{N-1} g(T^k(x)) = \int_{\mathcal{M}} g d\mu. \quad (3)$$

The left-hand side of (3) is known as the *time-average* of a function $g \in C(\mathcal{M})$ whereas the right-hand side of (3) is known as the *space average*. It follows Birkhoff’s pointwise ergodic theorem [14, Theorem 2.30] that the time-average of any $g \in C(\mathcal{M})$ necessarily exists on a set of full μ -measure. To formally discuss the statistical properties of dynamical trajectories, we now define the N -step *occupation measure* given the initial condition $x \in \mathcal{M}$ as

$$\mu_{x,N}(B) := \frac{1}{N} \sum_{k=0}^{N-1} \chi_B(T^k(x)), \quad \forall B \in \mathcal{B}. \quad (4)$$

As noted in [14, Definition 4.19], the condition that a point $x \in \mathcal{M}$ is generic is equivalent to the condition

$$\lim_{N \rightarrow \infty} \mu_{x,N} = \mu, \quad (5)$$

where convergence takes place in the weak-* topology. Since the quantity $\mu_{x,N}(B)$ approximates the average amount of time for which the *orbit* $\{T^k(x)\}_{k=0}^{\infty}$ initiated at $x \in \mathcal{M}$ resides in a measurable set $B \in \mathcal{B}$, this convergence indicates that the collection of generic points all share the same asymptotic statistical behavior.

When the measure μ is *ergodic* (see [14, Definition 2.13]), it holds that μ -almost every $x \in \mathcal{M}$ is a generic point [14, Corollary 4.20]. However, if μ is an ergodic measure that is singular with respect to the Lebesgue measure, the resulting collection of generic points may be physically insignificant and difficult to observe computationally. Motivated by this perspective, an invariant measure μ is said to be *physical* if there exists a collection of generic points with positive Lebesgue measure [66, Definition 2.3]. Physical measures are closely related to so-called *Sinai–Ruelle–Bowen (SRB) measures* [9, 66], and in the case of Axiom A attractors where $T \in C^2(\mathcal{M}, \mathcal{M})$, the two have been shown to coincide [66, Theorem 1]. Importantly, the existence of a physical measure cannot provide insight into the complexity of the dynamics for the set of generic points. However, as noted in [66], an SRB measure with nonzero *Lyapunov exponents* [19, Chapter 1] is a particular type of physical measure that describes chaotic attractors.

We will next discuss the ways in which a physical invariant measure μ can be computationally approximated. If one collects the measurements $\{T^k(x)\}_{k=1}^N$, the weak-* convergence in (5) suggests that the physical measure μ will describe the statistics of our measurements provided that N is sufficiently large. Motivated by this perspective, we can discretize the domain \mathcal{M} and directly compute the occupation measure (4) for each cell in the discretization to approximate the physical measure. This procedure is illustrated in Figure 1 and has been previously used to approximate physical measures in [1, 21, 65].

Other approaches have been proposed to compute the invariant measure as the stationary vector of the finite-dimensional approximation of the continuous *Frobenius–Perron* operator [34], including Ulam’s method [19] and Galerkin-type

methods [10, 33]. More precisely, these discretizations are used to construct a Markov matrix that represents a random dynamical system approximating the deterministic map $T : \mathcal{M} \rightarrow \mathcal{M}$. An invariant measure for the discrete approximation is then recovered as a stationary vector of the resulting Markov matrix. As the discretization is refined, certain assumptions guarantee that the desired SRB measure will be recovered in the weak-* limit [10, Theorem 4.14]. The process of identifying SRB measures as so-called *zero-noise limits* has also led to theoretical results which prove their existence for certain classes of dynamical systems [9]. Though we have reviewed the theory of physical measures and SRB measures in the context of arbitrary discrete-time dynamical systems, we will hereafter focus on applications in which the dynamics are given by a time- Δt flow map for some $\Delta t > 0$.

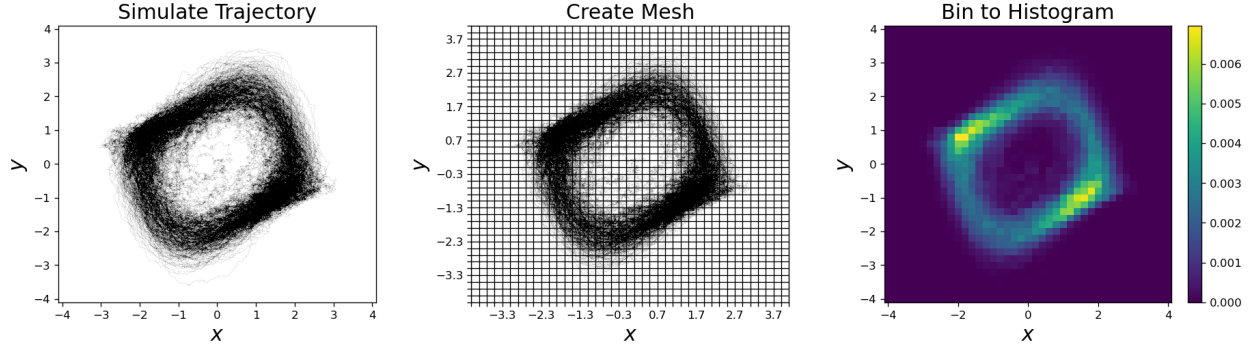


Figure 1: To computationally approximate a physical measure without knowledge of the dynamical system’s functional form or the sampling times of trajectory data, the following procedure is used. We first obtain trajectory measurements (left), then form a finite mesh over the state space (middle), and lastly bin the sampled trajectory to a histogram (right) to represent the probability of occupation for each cell in the discretization of the state space.

2.2 Stochastic Dynamics and the Fokker–Planck Equation

Consider an Itô stochastic differential equation (SDE) of the form

$$dX_t = v(X_t)dt + \sigma(X_t)dW_t, \quad X_0 = x. \quad (6)$$

Above, W_t is a Brownian motion, v is the velocity, and σ determines the diffusion matrix $\Sigma(\mathbf{x}) = \frac{1}{2}\sigma(\mathbf{x})\sigma(\mathbf{x})^\top$. For simplicity, we will consider the case of a constant diffusion. Similar to the deterministic setting, there are analogous notions of invariant measures, ergodicity, and physical measures in the stochastic setting [4, 24]. One may use the Euler–Maruyama method to obtain the numerical solution to (6) on the time interval $[0, T]$,

$$X_{j+1} = X_j + v(X_j)\Delta t + \sigma(X_j)\xi_j\sqrt{\Delta t}, \quad \Delta t := T/N, \quad j \in \{0, \dots, N-1\},$$

where $\{\xi_j\}$ are independently and identically distributed (i.i.d.) from $\mathcal{N}(0, I)$, the standard normal distribution on \mathbb{R}^d .

The Fokker–Planck equation provides a PDE description of the probability density $\rho(\mathbf{x}, t)$ of the random variable X_t . By [53, Page 88], the density evolves as

$$\frac{\partial \rho(\mathbf{x}, t)}{\partial t} = -\nabla \cdot (\rho(\mathbf{x}, t)v(\mathbf{x})) + \nabla \cdot (\nabla \cdot (\Sigma(\mathbf{x})\rho(\mathbf{x}, t))). \quad (7)$$

By assuming a constant diffusion, we may write $\Sigma(\mathbf{x}) = DI$, where I denotes the identity and $D > 0$ is a constant representing the scale of the diffusion. Equation (7) can then be simplified to read

$$\frac{\partial \rho(\mathbf{x}, t)}{\partial t} = -\nabla \cdot (\rho(\mathbf{x}, t)v(\mathbf{x})) + D\nabla^2 \rho(\mathbf{x}, t). \quad (8)$$

We leave the study of a non-constant or anisotropic diffusion for later work. We remark that if $D = 0$, (8) reduces to the so-called continuity equation, which instead models the probability flow of the ODE given by $\dot{\mathbf{x}} = v(\mathbf{x})$. Under certain conditions [27], the steady-state solution $\rho(\mathbf{x})$ of (8) exists and satisfies

$$\nabla \cdot (\rho(\mathbf{x})v(\mathbf{x})) = D\nabla^2 \rho(\mathbf{x}). \quad (9)$$

Since (9) describes a limiting distribution $\lim_{t \rightarrow \infty} \rho(\mathbf{x}, t)$, it has been previously used to provide approximations of invariant measures for stochastically-forced dynamical systems [1].

2.3 Delay Coordinates and Takens' Theorem

The technique of *time-delay embedding* is a popular approach for reconstructing chaotic dynamical systems from limited observations and has found numerous applications in the physical sciences [5, 21, 32, 58]. The procedure involves embedding time series measurements $\psi(t) = \psi(\mathbf{x}(t))$ of a full state $\mathbf{x}(t)$ into d -dimensional Euclidean space by considering the vector of time-lagged measurements $\Psi_{d,\tau}(t) = (\psi(t), \psi(t-\tau), \dots, \psi(t-(d-1)\tau))$, for some $\tau > 0$. Takens' theorem [59] provides suitable assumptions under which $\Psi_{d,\tau}(t)$ and $\mathbf{x}(t)$ are related via a diffeomorphism, implying that the time-lagged vector of partial observations $\Psi_{d,\tau}(t)$ is sufficient for reconstructing the full state $\mathbf{x}(t)$. Notably, the embedding dimension provided in [59] is $d = 2m + 1$ where m is the dimension of a compact manifold \mathcal{M} on which the flow map f_t for the original dynamics is defined. In cases when trajectories are attracted to a compact subset A with *box-counting dimension* (see [56, Page 586]) d_A strictly less than m , it turns out that lower-dimensional reconstructions can be obtained.

Indeed, it was shown in [56, Theorem 2.5] that for an open subset $U \subset \mathbb{R}^k$, a flow $f_t : U \rightarrow \mathbb{R}^k$, and a compact subset $A \subset U$ with box-counting dimension d_A , suitable assumptions on the equilibria and periodic points of f_t guarantee that for almost all C^1 observation functions $\psi : U \rightarrow \mathbb{R}$, the mapping $\Psi_{d,\tau}(\mathbf{x}) = (\psi(\mathbf{x}), \psi(f_{-\tau}(\mathbf{x})), \dots, \psi(f_{-(d-1)\tau}(\mathbf{x})))$ is one-to-one on A , where d is an integer strictly larger than $2d_A$. Moreover, the mapping $\Psi_{d,\tau}(\cdot)$ preserves any manifold structure on A , i.e., it is an immersion for all compact subsets C of a smooth manifold which is contained within A . This result is a helpful generalization of Takens' theorem, as the box counting dimension for chaotic attractors can be much smaller than the dimension of Euclidean space on which their flows are defined [55, Example 3.2.4].

When a time-series projection $\psi(t)$ of an unknown system $\dot{\mathbf{x}} = v(\mathbf{x})$ is observed, one can try to numerically determine a suitable embedding dimension d and time delay τ ; see for example [7, 40, 42, 62]. Choosing a proper embedding dimension and time delay is important for obtaining a reliable surrogate model of the original dynamics in time-delayed coordinates. Notably, in Section 5.2, we demonstrate that models for the velocity in time-delayed coordinates can incur excess uncertainties when the embedding dimension is not sufficiently large.

2.4 Prior Work on Learning Dynamics from Invariant Measures

For chaotic systems, trajectories are sensitive to initial conditions and estimation parameters. Sometimes, the approximated reference velocity field $\{\hat{v}(\mathbf{x}(t_i))\}$ cannot be accurately estimated from trajectory $\{\mathbf{x}(t_i)\}$ due to the lack of observational data, slow sampling, discontinuous or inconsistent time trajectories, and noisy measurements. To tackle such difficulties, instead of working with the Lagrangian trajectories, [21, 65] propose an Eulerian approach by treating the occupation measure (4) as the data. When enough samples are available, the occupation measure can be treated as an approximation to the invariant measure; see Section 2.1. Finding the optimal parameter θ is then translated into the optimization problem (2). The reference measure ρ^* is the occupation measure converted from the observed trajectories $\{\hat{\mathbf{x}}(t_i)\}$; see Figure 1. In [21], the approximated synthetic $\rho_\varepsilon(v(\theta))$ is generated by first simulating the synthetic trajectories $\{\mathbf{x}(t_i; \theta)\}$ based on the dynamical system and then computing its histogram following (4). Since this approach requires lengthy trajectory simulation, each evaluation of $\rho_\varepsilon(v(\theta))$ for a given θ is relatively costly. Moreover, it is difficult to compute the derivative of $\rho_\varepsilon(v(\theta))$ with respect to θ , due to the histogram approximation of nonlinear trajectories. As an improvement to the original idea in [21], [65] proposes a surrogate model to approximate $\rho_\varepsilon(v(\theta))$ that is differentiable in θ and sometimes faster to compute. The key idea is to solve for $\rho_\varepsilon(v(\theta))$ as the distributional steady-state solution to the continuity equation (i.e., (9) with $D = 0$) using a finite volume upwind scheme together with the teleportation regularization. The gradient of the objective function \mathcal{J} in (2) with respect to the parameter θ can be efficiently computed based on the adjoint-state method [65, Sec. 5].

The task of learning a dynamical system from an invariant measure has also been studied in the discrete-time setting under the inverse Frobenius–Perron problem [45, 51, 54, 64]. The Frobenius–Perron operator, also known as the transfer operator, characterizes the time-evolution of an initial measure μ_0 according to some prespecified dynamical system. Given a probability measure μ , the inverse Frobenius–Perron problem seeks to construct a dynamical system for which μ is a fixed point of the associated transfer operator. The most widely studied case involves recovering an ergodic map T on $[0, 1]$ for which a prescribed absolutely continuous measure is the unique fixed point of the discrete transfer operator. In this particular setting, various approaches such as topological conjugation [22] and matrix methods [50] have been introduced to solve the inverse problem. The multivariate inverse Frobenius–Perron problem was also studied in [18], where ergodic maps were constructed to adhere to the statistics of two-dimensional densities. Moreover, due to inherent non-uniqueness in the inverse problem, recent approaches further restrict the solution space of the discrete ergodic maps to those with a prescribed power spectrum [44]. To the best of our knowledge, [65] and our contributions here are the first works that numerically solve the inverse Frobenius–Perron problem in the continuous-time setting. Moreover, we do not assume that μ is absolutely continuous, as we use a finite-volume discretization to approximate the Frobenius–Perron operator.

3 The Forward Model and Modeling Errors

A central contribution of this work is to consider a different regularized forward model than the one in [65], especially for trajectory measurements containing intrinsic noise which can be interpreted as sample paths of stochastic dynamical systems (6). In those cases, the Fokker–Planck equation (7) is a better candidate as the PDE surrogate model, as it contains a diffusion term which can fit noise present in the data. Based on the relationship between (6) and (7), one can learn both the velocity field $v(\mathbf{x})$ and the diffusion tensor $\Sigma(\mathbf{x})$ in the optimization framework (2). For simplicity, we only consider a fixed diffusion constant and leave the investigation of multi-parameter inversion to future work.

We will use (9) as the forward model to fit invariant measures generated by trajectories with intrinsic noise. While, the diffusion term allows the model to fit the intrinsic noise and prevent over-fitting the noise into the target velocity component, it also controls the scaling of the reconstructed velocity $v(\mathbf{x}; \theta)$. Indeed, when $D = 0$ and $\tilde{v}(\mathbf{x}) = a v(\mathbf{x})$, we have $\nabla \cdot (\rho(\mathbf{x})\tilde{v}(\mathbf{x})) = 0$ as long as $\nabla \cdot (\rho(\mathbf{x})v(\mathbf{x})) = 0$, for any $a > 0$. However, for most cases, \tilde{v} and v will not solve the stationary Fokker-Planck equation (9) for $D > 0$.

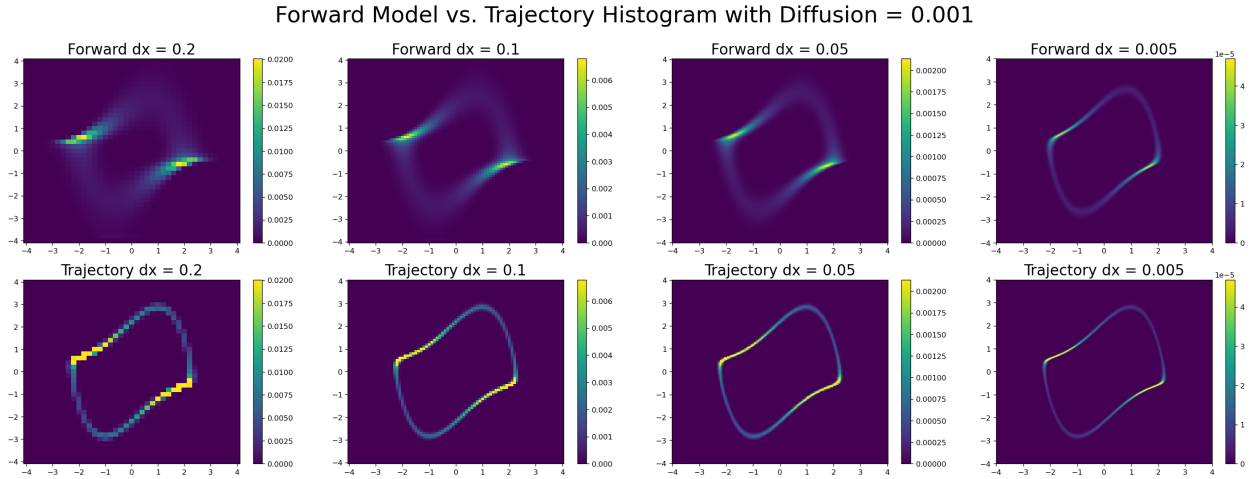


Figure 2: As the mesh size of the forward model discretization is refined, we visually observe the convergence of the computed steady-state solution to (9) (top row) to the approximate physical measure obtained by binning a time trajectory based on the SDE (6) (bottom row). The Van der Pol oscillator (18) with $c = 1$ is used in this example, and the histograms indicate mass-per cell.

3.1 Finite Volume Discretization

We assume that our system evolves on the d -dimensional rectangular state space $\Omega = [a_1, b_1] \times \dots \times [a_d, b_d] \subset \mathbb{R}^d$, with a spatially dependent velocity $v : \Omega \rightarrow \mathbb{R}^d$. We define $n_i \in \mathbb{Z}^+$, $1 \leq i \leq d$, to be the number of equally-spaced points along the i -th spatial dimension at which we wish to approximate the solution of (8), as well as the mesh spacing $\Delta x_i := \frac{b_i - a_i}{n_i - 1}$. We are interested in obtaining a solution to the forward problem at points of the form

$$x_{k_1, \dots, k_d} := \left(a_1 + k_1 \Delta x_1, \dots, a_d + k_d \Delta x_d \right) \in \Omega, \quad k_i \in \{1, \dots, n_i\}.$$

We will index our coordinates using column-major order and write $x_{k_1, \dots, k_d} = x_j$ where

$$j = k_1 + \sum_{i=2}^d (k_i - 1) S_i, \quad S_i := \prod_{j=1}^{i-1} n_j. \quad (10)$$

We will regard x_j as the center of the cell C_j where

$$C_j = \prod_{i=1}^d \left[a_i + \left(k_i - \frac{1}{2} \right) \Delta x_i, a_i + \left(k_i + \frac{1}{2} \right) \Delta x_i \right) \subset \Omega.$$

Following the approach in [3], we implement a first-order upwind finite volume discretization of the continuity equation, adding a diffusion term using the central difference scheme and enforcing a zero-flux boundary condition [36].

This allows us to obtain an explicit time-evolution of the probability vector $\rho = [\rho_1 \ \rho_2 \ \dots \ \rho_N]^\top \in \mathbb{R}^N$, where $N = \prod_{i=1}^d n_i$. While ρ is a discrete probability measure over the cells C_j , it also corresponds to a piecewise-constant probability density function on Ω . With an abuse of notation, we will refer to both the piecewise-constant density and the discrete probability measure as ρ . We discretize the time domain with a step size Δt chosen to satisfy the Courant–Friedrichs–Lewy (CFL) stability condition [36, Chapter 20]. Based on (8), the probability vector at the l -th time step evolves as

$$\rho^{(l+1)} = \rho^{(l)} + K\rho^{(l)}, \quad K = \sum_{i=1}^d \frac{\Delta t}{\Delta x} K_i,$$

where each K_i is a tridiagonal matrix given by

$$K_i := \begin{matrix} S_i \left\{ \begin{array}{cccc} \ddots & & & \\ & -v_{j-1}^{i,-} + \frac{D}{\Delta x_i} & & \\ & \vdots & & \\ & v_{j-1}^{i,-} - w_{j-1}^{i,+} - \frac{2D}{\Delta x_i} & -v_j^{i,-} + \frac{D}{\Delta x_i} & \\ \ddots & \vdots & \vdots & \\ & w_{j-1}^{i,+} + \frac{D}{\Delta x_i} & v_j^{i,-} - w_j^{i,+} - \frac{2D}{\Delta x_i} & -v_{j+1}^{i,-} + \frac{D}{\Delta x_i} \\ & & \vdots & \vdots \\ & & w_j^{i,+} + \frac{D}{\Delta x_i} & v_{j+1}^{i,-} - w_{j+1}^{i,+} - 2\frac{D}{\Delta x_i} \\ & & & \vdots \\ & & & w_{j+1}^{i,+} + \frac{D}{\Delta x_i} \\ & & & \ddots \\ & & & \ddots \end{array} \right. \end{matrix} \in \mathbb{R}^{N \times N}.$$

Above, we have defined for each $j \in \{1, \dots, N\}$ the upwind velocities

$$\begin{aligned} v_j^{i,-} &:= \min\{0, v_j^i\}, & v_j^{i,+} &:= \max\{0, v_j^i\}, \\ w_j^{i,-} &:= \min\{0, w_j^i\}, & w_j^{i,+} &:= \max\{0, w_j^i\}, \end{aligned}$$

where $v_j^i := v(x_j - \mathbf{e}_i \Delta x_i / 2) \cdot \mathbf{e}_i$ and $w_j^i := v(x_j + \mathbf{e}_i \Delta x_i / 2) \cdot \mathbf{e}_i$ denote the i -th components of the velocity field at the center of cell faces, and $\{\mathbf{e}_i\}$ is the standard basis in \mathbb{R}^d . We remark that if x_j is away from $\partial\Omega$, then $w_j^{i,\pm} = v_{j+1}^{i,\pm}$. To enforce the zero-flux boundary condition, we set both the velocity v and diffusion D to be zero on $\partial\Omega$. As a result, the columns of K each sum to zero, and the total probability

$$\rho^{(l)} \cdot \mathbf{1} = 1, \quad \mathbf{1} := [1 \ \dots \ 1]^\top \in \mathbb{R}^N,$$

is conserved under time-evolution. Since numerical artifacts cause the flux accumulation along the boundary, we also enforce $\rho = 0$ on $\partial\Omega$. When the boundary $\partial\Omega$ is sufficiently far from the trajectory data, this artifact is insignificant. Hereafter, we assume the uniform spatial discretization $\Delta x_i = \Delta x$ for all $i = 1, \dots, d$. For a complete description of the finite volume scheme, we refer to [36]. We remark that there are many higher-order structure-preserving schemes to solve (8); see [26] for example. A more accurate numerical scheme can further reduce the forward modeling error.

3.2 Teleportation and Diffusion Regularization

We use the finite volume discretization of the Fokker–Planck equation in Section 3.1 to approximate its steady-state solution. After discretization, finding such stationary distributions to (9) is equivalent to solving the linear system

$$\rho = K\rho + \rho \iff (I + K)\rho = \rho.$$

Since the columns of K sum to zero, we have that $M := I + K$ is a column-stochastic Markov matrix. When $D \neq 0$, M is a transition matrix for an ergodic Markov chain, which has a unique equilibrium. When $D = 0$, to guarantee the uniqueness of the equilibrium, [65] applies the so-called teleportation regularization [20] and considers

$$M_\varepsilon := (1 - \varepsilon)M + \varepsilon U, \quad U = N^{-1} \mathbf{1} \mathbf{1}^\top \in \mathbb{R}^{N \times N}.$$

There is now a unique solution to the linear system

$$M_\varepsilon \rho = \rho, \quad \rho \cdot \mathbf{1} = 1, \quad \rho > 0. \quad (11)$$

From a computational aspect, it is useful to take advantage of the fact that $M - I$ is sparse where $I \in \mathbb{R}^{N \times N}$ is the identity matrix, and to instead solve

$$(1 - \varepsilon)(M - I)\rho = -N^{-1}\varepsilon\mathbf{1},$$

where we have simply rearranged terms in (11) and used the fact that $\rho \cdot \mathbf{1} = 1$.

Since U is also a column stochastic Markov matrix with the uniform probability of visiting any point of the mesh, using M_ε amounts to stopping the dynamics based on M at a random time and restarting it from a uniformly randomly chosen initial point. The size of ε represents the restarting frequency—the smaller ε , the rarer we restart [65].

On the other hand, adding the diffusion component D to the tridiagonal matrix K can be seen as another way of regularizing the noise-free Markov matrix by adding a scaled Brownian motion after each discrete evolution of the deterministic dynamics. For deterministic dynamics with $D = 0$, the solution to (9) might not be unique if there is more than one attractor. The use of teleportation connects all attractors through the “random restart”, and the solution ρ_ε to the linear system (11) has support that connects all the disjoint attractors. Similarly, when $D \neq 0$, the Brownian motion connects all disjoint attractors of the deterministic dynamics, giving a unique steady-state solution. In this scenario, the use of teleportation for the diffusive case is simply a numerical treatment to improve the conditioning of matrix M rather than to guarantee the uniqueness of ρ .

It is worth noting that both the teleportation regularization and an incorrect diffusion coefficient could be sources of modeling error when we perform parameter identification. Although these regularizations enable faster evaluation of $\rho_\varepsilon(v(\theta))$ and better posedness of the forward problem, they may reduce the accuracy of the inverse problem solution.

3.3 Numerical Diffusion

In Figure 2, we illustrate the ρ_ε computed as the steady-state solution to the Fokker–Planck equation in the top row and the approximation to physical invariant measures of the corresponding SDE in the bottom row. From Figure 2, we see that on a coarse mesh, the first-order finite volume scheme incurs a lot of numerical error, which gives a computed solution with an artificial diffusion effect and thus is often referred to as the numerical diffusion [3]. The amount of numerical diffusion is reduced as the mesh is refined since it is incurred by the first-order scheme, which is expected to decay as $\mathcal{O}(\max_i \Delta x_i)$ in the L^∞ norm as we refine the mesh [36]. Besides the teleportation and the modeling diffusion D , the presence of numerical diffusion is another modeling error incurred from solving the forward problem.

4 Gradient Calculation & Velocity Parameterization

Another main contribution of this paper is to reconstruct the velocity field $v(\mathbf{x})$ using large-scale parameterizations $v(\mathbf{x}; \theta)$, which turns an infinite-dimensional problem of searching for $v(\mathbf{x})$ in a function space to a finite-dimensional optimization problem of finding $\theta \in \Theta \subset \mathbb{R}^m$. Here, we introduce parameterizations based on piecewise-constant, neural network, and global polynomial functions. We also investigate various data-fitting objective functions \mathcal{J} that compare the mismatch between the observed and simulated invariant measures, ρ^* and $\rho_\varepsilon(v(\theta))$. We compute the gradient of such functions with respect to the coefficients θ in the parameterized velocity model $v(\mathbf{x}; \theta)$ based on the adjoint-state method for the PDE-constrained part and the backpropagation technique [35] for the neural network part. Thanks to these techniques, we can then efficiently evaluate the gradients of \mathcal{J} with respect to θ and thus conveniently use gradient-based optimization algorithms to iteratively update θ , e.g., steepest descent, L-BFGS, conjugate gradient descent methods as well as stochastic methods such as Adam [31]. For notational simplicity, we will write $\rho(v(\theta)) = \rho_\varepsilon(v(\theta))$ throughout this section.

4.1 Gradient Calculation Through the Adjoint-State Method

Recall the finite volume scheme in Section 3.1 for solving (9). The forward model yields a discrete measure $\rho(v(\theta)) = \rho(\theta) = [\rho_1(\theta) \dots \rho_j(\theta) \dots \rho_N(\theta)]^\top$ over the cells $\{C_j\}$, which converges to the solution to (9) in the weak sense as we refine the discretization parameters. For the explicit form of $\rho(v(\theta))$, we refer to [65, Eqn. (5.1)]. Note that we have highlighted the dependence of our approximate steady-state distributional solution to the Fokker–Planck equation (9) on the velocity $v(\mathbf{x}; \theta)$. Our goal is to solve the optimization problem (2):

$$\inf_{\theta \in \Theta} \mathcal{J}(\rho(v(\theta)), \rho^*)$$

by using gradient-based methods, where \mathcal{J} is the cost function, and ρ^* represents our inference data. The *adjoint-state method* is an efficient technique by which we can evaluate the derivative $\partial_\theta \mathcal{J}$, as the computation time is largely

independent of the size of θ . One can derive the adjoint-state method for gradient computations by differentiating the discrete constraint [52], which in our case is the eigenvector problem

$$g(\rho(\theta), \theta) = M_\varepsilon(\theta)\rho(\theta) - \rho(\theta) = \mathbf{0},$$

where $\rho(\theta) \cdot \mathbf{1} = 1$. Specifically, we will compute $\partial_\theta \mathcal{J} = \lambda^\top \partial_\theta g$ where λ solves $(\partial_\rho g)^\top \lambda = -(\partial_\rho \mathcal{J})^\top$. In our case, this linear system is the adjoint equation [65, Eqn. (5.8)]

$$(M_\varepsilon^\top - I)\lambda = -(\partial_\rho \mathcal{J})^\top + (\partial_\rho \mathcal{J})^\top \rho \mathbf{1}, \quad (12)$$

and the derivative

$$\partial_\theta \mathcal{J} = \lambda^\top (\partial_\theta M_\varepsilon) \rho. \quad (13)$$

As a result, we only need to compute the derivatives $\partial_\rho \mathcal{J}$ and $\partial_\theta M_\varepsilon$ to determine the gradient $\nabla_\theta \mathcal{J} = (\partial_\theta \mathcal{J})^\top$. The former depends on the choice of the objective function, while the latter is based on a specific parameterization of the velocity field $v(\mathbf{x}; \theta)$ determined by its hypothesis space.

4.1.1 The Computation of $\partial_\rho \mathcal{J}$

For the objective function \mathcal{J} , we consider the quadratic Wasserstein distance, the squared L^2 norm, the Kullback–Leibler (KL) Divergence, and the Jensen–Shannon (JS) Divergence.

Quadratic Wasserstein Distance: For probability measures ρ and ρ^* on Ω , with finite second-order moments, the squared quadratic Wasserstein distance is defined by

$$W_2^2(\rho, \rho^*) := \inf_{T_{\rho, \rho^*} \in \mathcal{T}} \int_\Omega |x - T_{\rho, \rho^*}(x)|^2 d\rho(x),$$

where $\mathcal{T} := \{T : \Omega \rightarrow \Omega : \rho(T^{-1}(B)) = \rho^*(B), \text{ for all measurable } B\}$ is the set of maps that push ρ forward into ρ^* [61]. With an abuse of notation, we also use $\rho(x)$ and $\rho^*(x)$ to denote the densities of ρ and ρ^* respectively. For efficient computation of the W_2 distance, we utilize the back-and-forth method [28], which instead uses the dual Kantorovich formulation [61]

$$W_2^2(\rho, \rho^*) = \sup_{\phi, \psi} \left(\int_\Omega \phi(x) \rho^*(x) dx + \int_\Omega \psi(x) \rho(x) dx \right),$$

where $\phi \in L_{\rho^*}^1(\Omega)$ and $\psi \in L_\rho^1(\Omega)$ are required to satisfy $\phi(x) + \psi(y) \leq |x - y|^2$. In this case, the Fréchet derivative of $\mathcal{J} = W_2^2(\rho, \rho^*)$ with respect to ρ is given by

$$\frac{\partial \mathcal{J}}{\partial \rho} = \psi.$$

Squared L^2 Norm: The squared L^2 distance as the objective function and its Fréchet derivative are given by

$$\mathcal{J} = \frac{1}{2} \int_\Omega |\rho(x) - \rho^*(x)|^2 dx, \quad \frac{\partial \mathcal{J}}{\partial \rho} = \rho - \rho^*.$$

KL-Divergence: The KL-divergence and its Fréchet derivative are given by

$$\mathcal{J} = D_{\text{KL}}(\rho, \rho^*) := \int_\Omega \rho^*(x) \log \left(\frac{\rho^*(x)}{\rho(x)} \right) dx, \quad \frac{\partial D_{\text{KL}}}{\partial \rho} = -\frac{\rho^*(x)}{\rho(x)}.$$

We remark that our definition of the KL-divergence differs from many applications in which it is commonly computed as $\mathcal{J} = D_{\text{KL}}(\rho^*, \rho)$.

JS-Divergence: Defining $\rho' := (\rho + \rho^*)/2$, the JS-divergence and its Fréchet derivative are given by

$$\mathcal{J} = D_{\text{JS}}(\rho, \rho^*) = \frac{1}{2} D_{\text{KL}}(\rho, \rho') + \frac{1}{2} D_{\text{KL}}(\rho^*, \rho'), \quad \frac{\partial D_{\text{JS}}}{\partial \rho} = \frac{1}{2} \log \left(\frac{2\rho}{\rho + \rho^*} \right).$$

Based on definitions of the KL and JS divergence, it is clear that we may encounter numerical instability issues if either ρ or ρ^* is not supported on the entire domain Ω . Thus, we remark that for the computation of both the KL and JS divergences, we restrict the domain Ω to regions where both ρ and ρ^* are strictly positive. This is equivalent to the definition of the KL and JS divergence based upon the so-called Csiszar divergence [57, Eqn. (1)].

4.2.1 Piecewise-Constant Parameterization

In the case of the piecewise-constant parameterization, we model the velocity as

$$v(\mathbf{x}; \theta) = \sum_{i=1}^d \sum_{j=1}^N v_j^i \chi_{C_j}(\mathbf{x}) \mathbf{e}_i, \quad \theta = \{v_j^i\}. \quad (16)$$

Here, we again use the column-major ordering from Section 3.1 to accumulate vectors of cells C_j with centers x_j , and velocity components,

$$v_j^i = v(x_j - \mathbf{e}_i \Delta x_i / 2) \cdot \mathbf{e}_i,$$

along the i -th direction of the cell face located at $x_j - \mathbf{e}_i \Delta x_i / 2$. The parameter space of the model presented in (16) is given by $\{v_j^i\}$, which has size $N \cdot d$, and the gradient of the parameters $\{v_j^i\}$ can be directly evaluated by (14).

We remark that (16) is only one variant of piecewise-constant parameterization since the parameterization mesh is the same as the discretization mesh in the finite-volume method; see Section 3.1. These two meshes do not have to be coupled together. To reduce the numerical error from the first-order scheme, it is preferable to reduce the spacing $\{\Delta x_i\}$, but we can keep the parameterization mesh fixed, so the size of the optimization problem does not change. In this case, we need to apply the chain rule (15) to obtain the final gradient after evaluating (14).

The model defined by (16) can be learned by gradient-based optimization methods. The regularity of the piecewise-constant model defined by (16) can be improved to a C^0 function by interpolating between the values v_j^i using either piecewise linear or higher-order piecewise polynomial functions, as in [38].

4.2.2 Global Polynomial Parameterization

Though the regularity of the piecewise-constant model given by (16) can be improved by interpolation, the inverted velocity $v(\mathbf{x}; \theta)$ may still be highly oscillatory if the mesh size Δx is small. Modeling approaches, such as SINDy [6], learn the velocity fields of dynamical systems from a polynomial basis together with sparse regression. Here, we show how the gradient derivation in (15) can be adapted to such polynomial basis parameterization of the velocity field

$$v(\mathbf{x}; \theta) = [v^1(\mathbf{x}; \theta), \dots, v^d(\mathbf{x}; \theta)]^\top = \sum_{i=1}^d v^i(\mathbf{x}; \theta) \mathbf{e}_i.$$

The i -th component of the velocity field $v^i(\mathbf{x}; \theta)$ parameterized by a linear combination of the monomial basis of degree at most K can be written as

$$v^i(\mathbf{x}; \theta) = \sum_{\ell=1}^M a_\ell^i (\mathbf{x}^\top \mathbf{e}_1)^{k_\ell^1} \dots (\mathbf{x}^\top \mathbf{e}_d)^{k_\ell^d}, \quad M = \binom{d+K}{K}, \quad \theta = \{a_\ell^i\}, \quad (17)$$

where the powers are represented by multi-indices $k_\ell^i = (k_\ell^1, \dots, k_\ell^d)$, $1 \leq \ell \leq M$, and $|k_\ell^i| \leq K$. The size of θ in this case is $d \cdot M$.

To learn the model parameterized by (17), we can use (15) to compute the gradient $\partial_{a_\ell^i} \mathcal{J}$. Without loss of generality, we assume $\Delta x_i = \Delta x$, for all $1 \leq i \leq d$. The only term in (15) which explicitly depends upon the velocity parameterization is

$$\frac{\partial v_j^i}{\partial a_\ell^i} = ((x_j - \mathbf{e}_i \Delta x / 2)^\top \mathbf{e}_1)^{k_\ell^1} \dots ((x_j - \mathbf{e}_i \Delta x / 2)^\top \mathbf{e}_d)^{k_\ell^d}, \quad 1 \leq j \leq N,$$

where i , a_ℓ^i and the multi-index k_ℓ^i are fixed. Note that $\partial_{a_\ell^i} v_j^{i'} = 0$ if $i' \neq i$. Thus, we can again use gradient-based methods to infer proper polynomial coefficients $\{a_\ell^i\}$.

Although a global polynomial parameterization guarantees ideal C^∞ regularity of the parameterized velocity $v(\mathbf{x}; \theta)$, the Runge phenomenon could be a potential downside of this approach. Specifically, as we increase the maximum degree K of the polynomial basis, we may encounter substantial interpolation errors near the boundary $\partial\Omega$.

4.2.3 Neural Network Parameterization

Motivated by the universal approximation theory of neural networks [25], we may also choose to model each component of the velocity $v^i(\mathbf{x}; \theta)$ as a feed-forward neural network, where the tunable parameters θ make up the network's weights

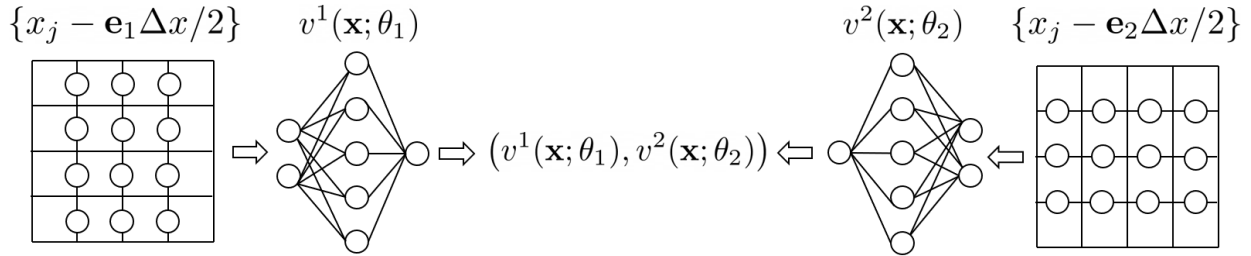


Figure 3: In two dimensions, both velocity components $v^1(\mathbf{x}; \theta_1)$ and $v^2(\mathbf{x}; \theta_2)$ are parameterized by fully connected neural networks with smooth activation functions. Due to the upwind finite volume method, the adjoint-state gradient calculation for $v^1(\mathbf{x}; \theta_1)$ is performed on the mesh $\{x_j - \mathbf{e}_1 \Delta x/2\}$, whereas the gradient calculation for $v^2(\mathbf{x}; \theta_2)$ is performed on the mesh $\{x_j - \mathbf{e}_2 \Delta x/2\}$. Both gradients are used in conjunction with backpropagation to train the networks, which ultimately yields a smooth map $\mathbf{x} \mapsto (v^1(\mathbf{x}; \theta_1), v^2(\mathbf{x}; \theta_2))$.

and biases. We follow [37] to combine the adjoint-state method for the PDE constraints and the backpropagation technique to update the weights and biases of the neural network.

The term $\partial_{v_j^i} \mathcal{J}$ in the gradient calculation (15) can be computed by first evaluating the neural network on the mesh of cell face centers oriented in the direction of \mathbf{e}_i to obtain $\{v_j^i\}$, which is then plugged into (14) to obtain $\partial_{v_j^i} \mathcal{J}$. Figure 3 illustrates where the neural network is evaluated for gradient computation. The remaining term $\partial_\theta v$ in (15) is then computed via the backpropagation technique [35].

For simplicity, we restrict ourselves to single-layer feed-forward networks. Moreover, by using a smooth activation function, such as the hyperbolic tangent or the sigmoid function, we can guarantee C^∞ regularity of the reconstructed velocity $v(\mathbf{x}; \theta)$ on the domain Ω . To enforce the zero-flux boundary condition, we manually set $v = 0$ on $\partial\Omega$. Consequently, the neural network parameterization may lack regularity near $\partial\Omega$. However, if the domain is sufficiently large, the support of the physical measure will be very far from $\partial\Omega$, in which case we will not observe any discontinuities originating from the boundary condition while simulating the trajectories based on (6). As we increase the number of nodes in the hidden layer of the neural network, both the approximation power and the potential difficulty of training the neural network are expected to increase.

5 Numerical Results

In this section, we present several numerical examples to demonstrate the utility of the proposed approach for learning dynamical systems from invariant measures with intrinsic noise¹. In Section 5.1, we study the inverse problem for the Van der Pol oscillator with a neural network parameterization of the velocity. In Section 5.2, we time-delay embed a signal sampled from a Hall-effect thruster and proceed to model the dynamics in delay-coordinates based upon the time-delayed invariant measure. We then illustrate that a very low-dimensional embedding will increase the uncertainty of the learned model and that the choice of parameterization largely affects the regularity of the reconstructed velocity. In Section 5.3, we study rolling averages of weekly temperature data and perform uncertainty quantification using the learned Fokker–Planck PDE in time-delayed coordinates. We conclude in Section 5.4 by inverting a component of the Lorenz-63 system’s velocity using a neural network parameterization.

5.1 Van der Pol Oscillator

We begin by considering the autonomous Van der Pol oscillator [23], given by

$$\begin{cases} \dot{x} = y, \\ \dot{y} = c(1 - x^2)y - x. \end{cases} \quad (18)$$

Our results for learning a dynamical system with prescribed statistical properties given by the stochastically-forced Van der Pol oscillator are shown in Figure 4. In the top row, the first panel features the velocity of (18) for the choice of $c = 0.5$, the second panel shows the approximate invariant measure from a diffuse trajectory simulated via the

¹For those interested, we also include an example Google Colaboratory file demonstrating the velocity inversion for a polynomial parameterization: <https://tinyurl.com/PDEinv>.

Euler–Maruyama method, the third panel shows the diffuse dynamics which were used to approximate the invariant measure, and the fourth panel shows the dynamics of the oscillator without stochastic forcing. Throughout, we color trajectories by their histogrammed density to illustrate the connection between the Lagrangian and Eulerian perspectives.

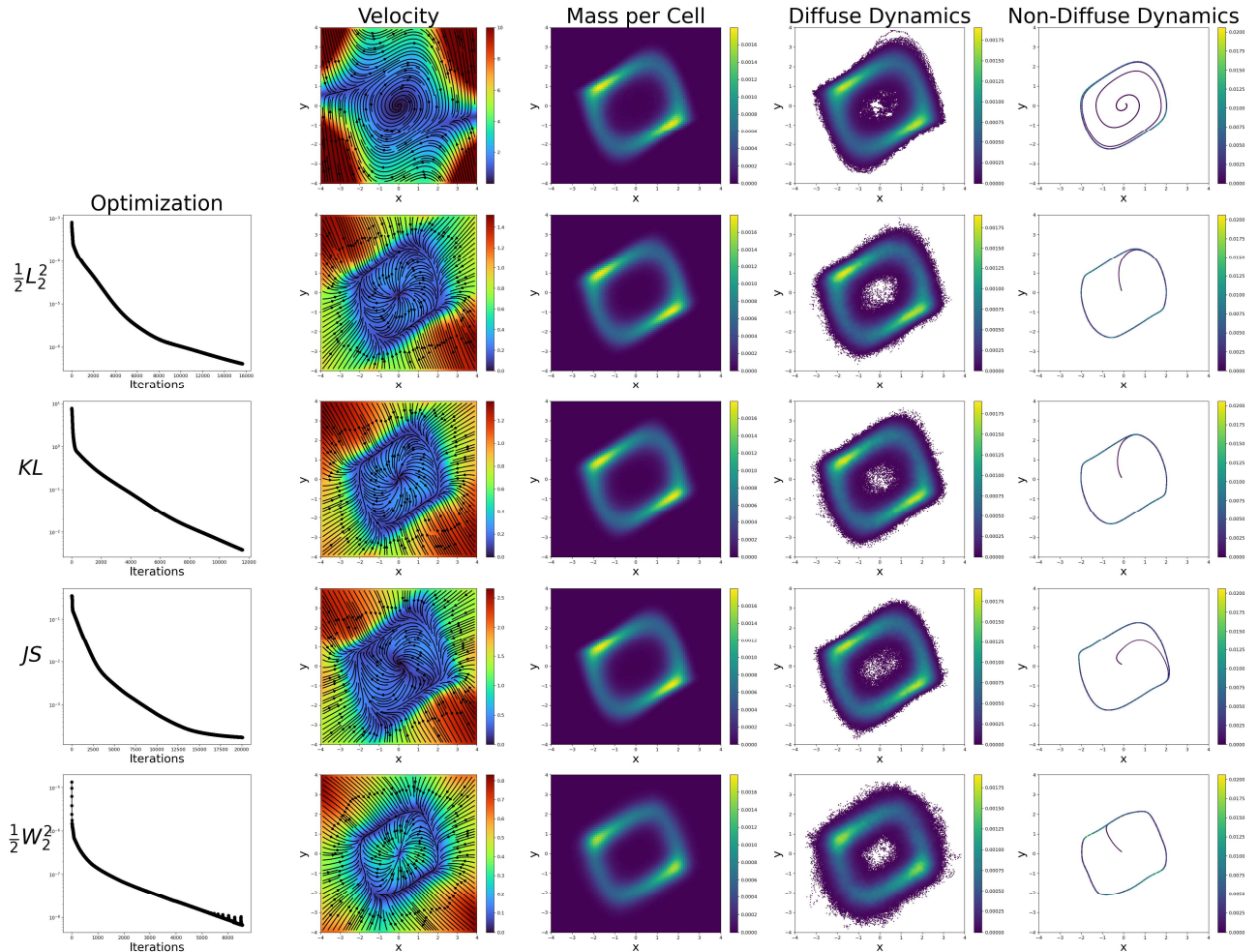


Figure 4: Learning velocity fields to reproduce the statistics of the stochastically-forced Van der Pol oscillator. The first row features the ground truth velocity, mass-per cell, and dynamics of the Van der Pol oscillator (18) with $c = .5$ and diffusion $D = .05$. The subsequent rows show the resulting optimization based on the observed density using each of the four objective functions studied in Section 4.1.1 along with a neural network parameterization utilizing a single hidden layer of 100 nodes and a hyperbolic tangent activation function. During the optimization, each objective function was reduced to .05% of its initial value. We emphasize that the density in the first row is approximated via the procedure in Figure 1, whereas the densities in the remaining rows are solutions of the PDE forward model from Section 3.1

In the following rows of Figure 4, we use a neural network parameterization to solve the inverse problem using the optimization framework from Sections 3.1 and 4. In the first column of Figure 4, we see that each objective function in Section 4.1.1 is reduced below .05% of its initial value. Moreover, the reconstructed velocity for each objective function is shown to vary significantly from the true velocity shown in the first row of Figure 4. This is largely due to the lack of data away from the main attracting limit cycle. In regions of the state space with no available data, we can only expect that the modeled velocity $v(x; \theta)$ will direct trajectories towards the attracting limit cycle on which the invariant measure is supported. Indeed, this is what we observe. Moreover, both the PDE forward model (9) and the statistics of the SDE simulation using the learned velocity match the ground truth invariant measure from the first row of Figure 4. These observations indicate that the learned velocity need not agree with the ground truth velocity to yield a dynamical system with the same invariant measure. Finally, in the last column of Figure 4, we approximate the noise-free limit cycle by removing the diffusion term in (6), which corresponds to the simulation of an ODE rather than an SDE.

To reduce the computational requirements of the inversion in the final row of Figure 4, we compute $\mathcal{J} = W_2^2$ on a coarsened mesh. Among the four objective functions in Figure 4, it is worth noting that the W_2 metric does not compare the two densities pointwisely and is well-defined for comparing singular measures, which is different from the other three. The distance reflects both the local intensity differences and the global geometry mismatches [16]. It has also been shown that the Wasserstein metric is robust to noise [12, 15]. Thanks to the geometric nature of the optimal transportation problem, the Wasserstein metric is primarily sensitive to global changes such as translation and dilation and is robust to small local perturbations such as noisy measurements of ρ^* . The better stability also brings a downside as the optimization landscape can be relatively flat around the ground truth, which may lead to compromised accuracy in the velocity reconstruction.

5.2 Hall-Effect Thruster

We now turn to the more realistic setting of experimentally sampled time-series data. Specifically, we study the Cathode–Pearson signal sampled from a Hall-effect thruster (HET) in its breathing mode. Hall-effect thrusters are in-space propulsion devices that exhibit dynamics resembling stable limit cycles while in breathing mode. For details about the experimental setup used to collect the data, the reader is encouraged to consult [13, 41]. In Section 5.2.1, we utilize Takens’ theorem [59] to reformulate the large-scale optimization framework presented in Sections 3 and 4 to be compatible with scalar time-series observations, and in Section 5.2.2 we demonstrate numerical results based upon this reformulation.

5.2.1 Methods

Intrinsic physical fluctuations present in the Cathode–Pearson signal indicate that the HET’s dynamics may be modeled well by a Fokker–Planck equation. Motivated by this insight, we first time-delay embed the Cathode–Pearson signal $C(t)$ in d -dimensions to form the trajectory $\mathbf{C}_{d,\tau}(t) := (C(t), C(t - \tau), \dots, C(t - (d - 1)\tau))$. We then use the procedure outlined in Figure 1 to compute the occupation measure ρ^* of $\mathbf{C}_{d,\tau}(t)$. By viewing each dimension of the coordinate system on which the measure ρ^* is supported as the independent variables $C_{-k\tau}(t) := C(t - k\tau)$ where $0 \leq k \leq d - 1$, we then seek a solution to the optimization problem (2) for a velocity $v = v(\mathbf{C}_{d,\tau}; \theta)$. Such a velocity can then provide us with a model of the asymptotic statistics of the embedded trajectory $\mathbf{C}_{d,\tau}(t)$, provided that a suitable diffusion coefficient can be found.

We note that forming the time-delay coordinates $\mathbf{C}_{d,\tau}(t)$ does require a knowledge of measurements at uniform increments in time. However, the available data may still be sampled slowly enough such that it is impractical to seek a direct approximation of the Lagrangian velocity through the standard approaches described in Section 1. This perspective motivates our use of the approach developed in Sections 3 and 4 to learn dynamical systems from invariant measures in time-delay coordinates.

Moreover, there are a few additional considerations which arise when adapting the modeling framework presented in Sections 3 and 4 to real-world data. Namely, we do not know the proper diffusion coefficient a priori (as was the case in Section 5.1). Moreover, the invariant measure that the model is based on does not contain any information about the time-scale at which the system evolves. Towards this, we utilize the following three-step procedure as a computationally efficient means to mitigating these difficulties.

1. Bin the trajectory $\mathbf{C}_{d,\tau}(t)$ onto a d -dimensional mesh with spacing Δx along each axis to form the occupation measure ρ^* , assume a constant diffusion coefficient $D > 0$, and learn the velocity $v = v(\mathbf{C}_{d,\tau}; \theta)$, using the framework from Sections 3 and 4.
2. Bin the trajectory $\mathbf{C}_{d,\tau}(t)$ onto another d -dimensional mesh with spacing $\Delta \hat{x} \leq \Delta x$ to create a new occupation measure $\hat{\rho}^*$ and adjust the diffusion coefficient by solving the optimization problem

$$\tilde{D} = \arg \min_{\hat{D} \in \mathbb{R}} \mathcal{J}(\rho_\varepsilon(v; \hat{D}), \hat{\rho}^*), \quad (19)$$

where the term $\rho_\varepsilon(v; \hat{D})$ in (19) denotes the forward model evaluation with the diffusion coefficient \hat{D} .

3. Rescale both the velocity and diffusion by solving the optimization problem

$$\tilde{a} = \arg \min_{a \in \mathbb{R}} \sum_{i=1}^N \left\| \hat{\mathbf{C}}(t_i; a) - \mathbf{C}_{d,\tau}(t_i) \right\|_2^2, \quad (20)$$

where $\hat{\mathbf{C}}(t_i; a)$ denotes the time- t_i solution of the ODE initial value problem with velocity $av(\cdot; \theta)$ and initial condition $\mathbf{C}_{d,\tau}(t_0)$. The final velocity and diffusion are then given by $\tilde{a}v(\cdot; \theta)$ and $\tilde{a}\tilde{D}$, respectively.

The three-step approach makes repeated use of the fact that $\rho_\varepsilon(v; D) = \rho_\varepsilon(av; aD)$, for any scalar multiple $a > 0$. Indeed, if the true diffusion coefficient $D^* > 0$ is unknown a priori, but we instead seek a solution $v(\cdot, \theta)$ with a different diffusion $D > 0$, it is guaranteed that the velocity $v = (D/D^*)v^*$ will still provide a solution to the inverse problem. This observation motivates step one, in which an arbitrary diffusion coefficient is used to find a solution $v(\cdot; \theta)$ to the inverse problem. As the dimensionality d is increased, solving the large scale optimization problem in step 1 on a fine mesh becomes infeasible. As such, step one is typically performed on a coarse mesh where additional Gaussian filtering is applied to the inference measure ρ^* to make the large-scale optimization more feasible.

The diffusion coefficient is then adjusted in step two on a finer mesh via (19) to mitigate the errors due to the Gaussian filtering, numerical diffusion, and histogram errors incurred during step one (see Figure 2). Finally, in step three the scale of both the velocity and diffusion are adjusted via (20) such that the time evolution of simulated trajectories is consistent with the inference trajectory $\mathbf{C}_{d,\tau}(t)$ in delay coordinates. Since diffusion plays a relatively small role over short time-scales for the quasi-periodic HET data, we use the trajectory to calibrate a reasonable time-scaling between our model and the available data. However, as the magnitude of the diffusion increases, the least squares fit in (20) will become less reliable and it may be preferable to instead minimize a transport cost between a collection of model samples and a collection of data samples at each time-step.

5.2.2 Results

The results of the three-step procedure in Section 5.2.1 for learning the HET dynamics are shown in Figure 5 for an embedding dimension of $d = 3$ and time-delay of $\tau = 1.4 \cdot 10^{-5}$ seconds, or rather $\tau = .23$ when normalizing the time-scale to the HET breathing mode frequency (16.6kHz). The modeled trajectory accurately reconstructs the shape of the embedded Cathode–Pearson signal but cannot capture the variable diffusion present throughout the time-delayed signal. We do not expect to capture such details, as we assume a constant diffusion coefficient in our model. Nevertheless, we regard the reconstruction of the 3D globally attracting limit cycle as a success and leave extending the model to account for the case of a non-constant diffusion tensor to future work.

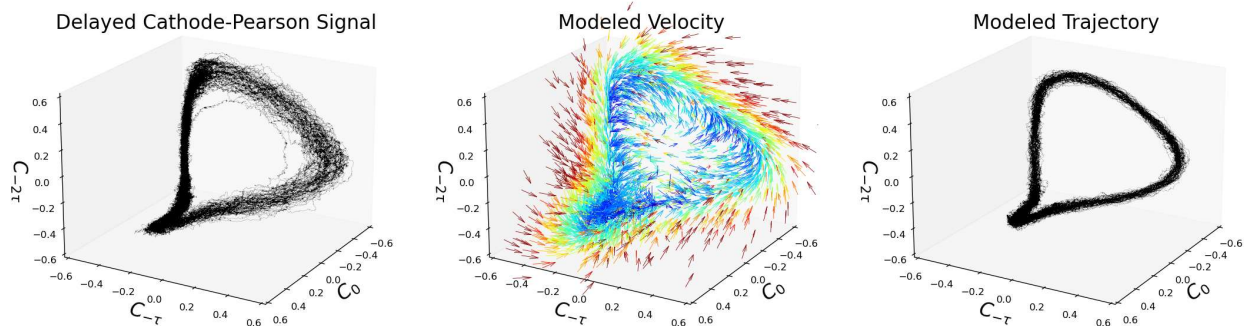


Figure 5: Learning the velocity from embedded Cathode–Pearson signal’s invariant measure. We present the time-delay embedded signal $\mathbf{C}_{3,\tau}(t)$ (left), the reconstructed velocity field from the embedded signal’s occupation measure (middle), where blue indicates slow speed and red indicates fast. Finally, we show a trajectory simulated with the Euler–Maruyama method from the learned velocity and diffusion (right). The velocity was parameterized by a neural network with 500 nodes in a single hidden layer and learned using the KL divergence loss function. The three-step procedure in Section 5.2.1 is used to learn the model, and in step one, additional Gaussian filtering is applied to the occupation measure ρ^* to simplify the resulting optimization.

The dimensionality of the original HET dynamics is unknown, and as such, a sufficient embedding dimension for the Cathode–Pearson signal is unclear, though likely very high. Interestingly, we can compare the model learned in Figure 5 with a 2D analog to demonstrate that when the number of time-delays is not sufficiently large, there is *more uncertainty* in modeling the time-delayed dynamics. This phenomenon is most evident when inspecting regions of the delayed Cathode–Pearson signal for which the 2D embedding lacks structure readily observed in 3D.

Specifically, consider a collection of nearby samples $\{\mathbf{C}_{3,\tau}(t_i)\}_{i=1}^n$ in the 3D time-delay coordinate system $(C_0, C_{-\tau}, C_{-2\tau})$. The corresponding 2D samples $\{\mathbf{C}_{2,\tau}(t_i)\}_{i=1}^n$ will also be nearby one another in the 2D time-delay coordinate system $(C_0, C_{-\tau})$. In Figure 6, we initiate uniform distributions centered about these samples in both 2D and 3D time-delay coordinate systems. We then evolve both the samples and initial uniform distributions forward in time. The evolution of the ground truth samples is simply determined by the time-delayed Cathode Pearson signal $\mathbf{C}_{d,\tau}(t)$, and the evolution of the uniform distributions is given by Fokker–Planck models constructed from the time-delayed Cathode Pearson signal’s invariant measure. As the modeled probability densities and ground truth

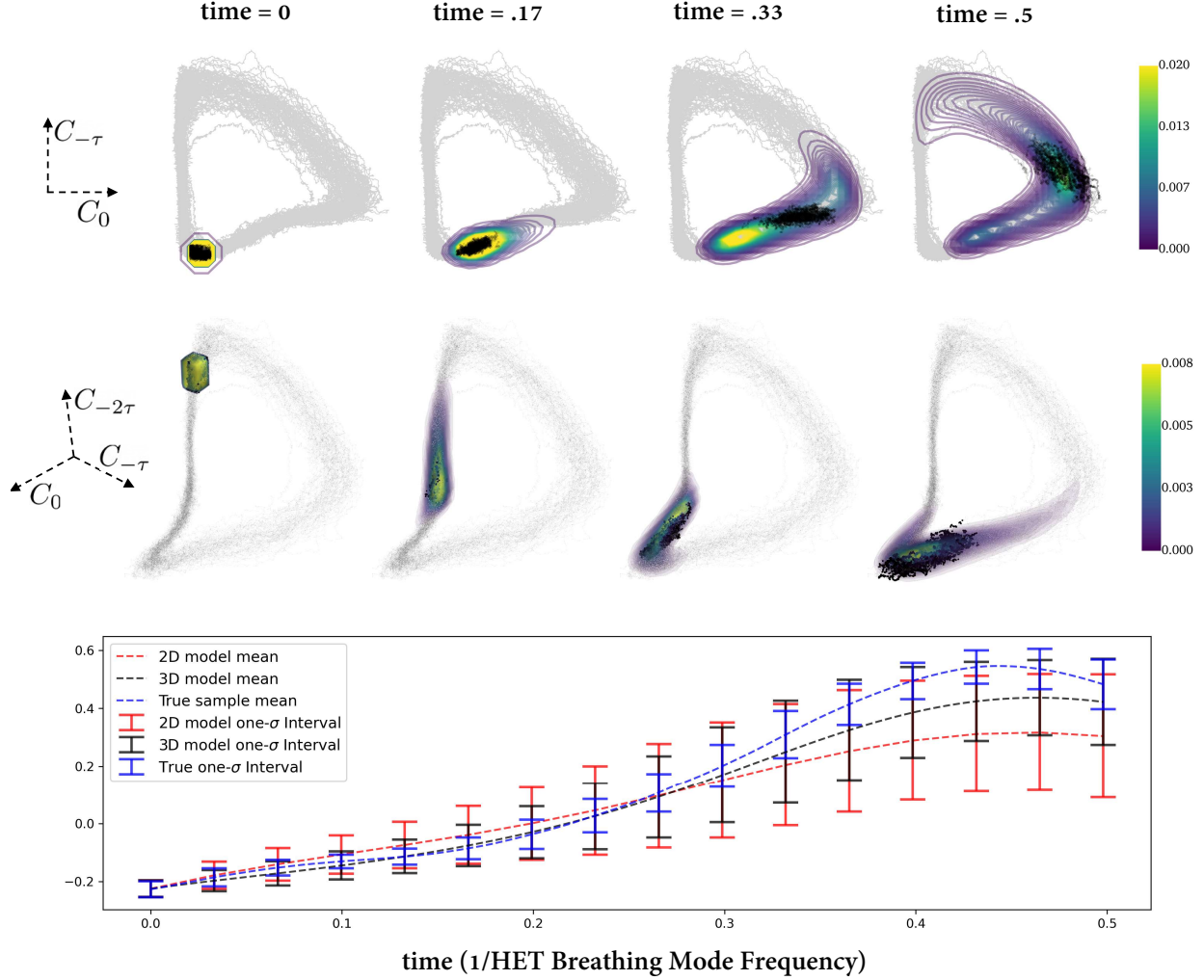


Figure 6: Comparing the model accuracy and uncertainty for the embedded Cathode–Pearson signal with 2D and 3D time delays. The time-evolution of the models is compared to a collection $\{C_{d,\tau}(t_i)\}_{i=1}^n$ of samples (plotted in black) from the time-delayed Cathode–Pearson signal. The first two rows feature four snapshots from the 2D and 3D models from the time interval $[0, .5]$. The bottom row compares the uncertainty of the models to the ground truth data. The time units are normalized to the inverse of a HET breathing mode frequency (16.6kHz). Both models utilized a neural network velocity parameterization with 500 nodes in a single hidden layer and reduced the KL divergence objective function to .1% of its initial value during training. As in Figure 5, the three-step procedure in Section 5.2.1 is used to learn the models, and in step one, additional Gaussian filtering is applied to the occupation measure ρ^* to simplify the resulting optimization. The 3D visualization was plotted using [55].

samples evolve in time, we observe in Figure 6 that the mean of the 3D model matches the true sample mean more closely than the 2D model, and that it has less uncertainty.

In Figure 7, we study the three parameterizations from Section 4.2 for learning the time-delayed Cathode–Pearson signal’s velocity, now with an embedding dimension of two to allow for clearer visualizations. It can be seen that the density associated with each velocity parameterization indeed matches the ground truth density in Figure 7, but that the velocity fields differ significantly from one another. The piecewise-constant velocity in Figure 7 suffers from poor regularity with discontinuities on the attracting limit cycle. As a result, we lose the connection between the Eulerian

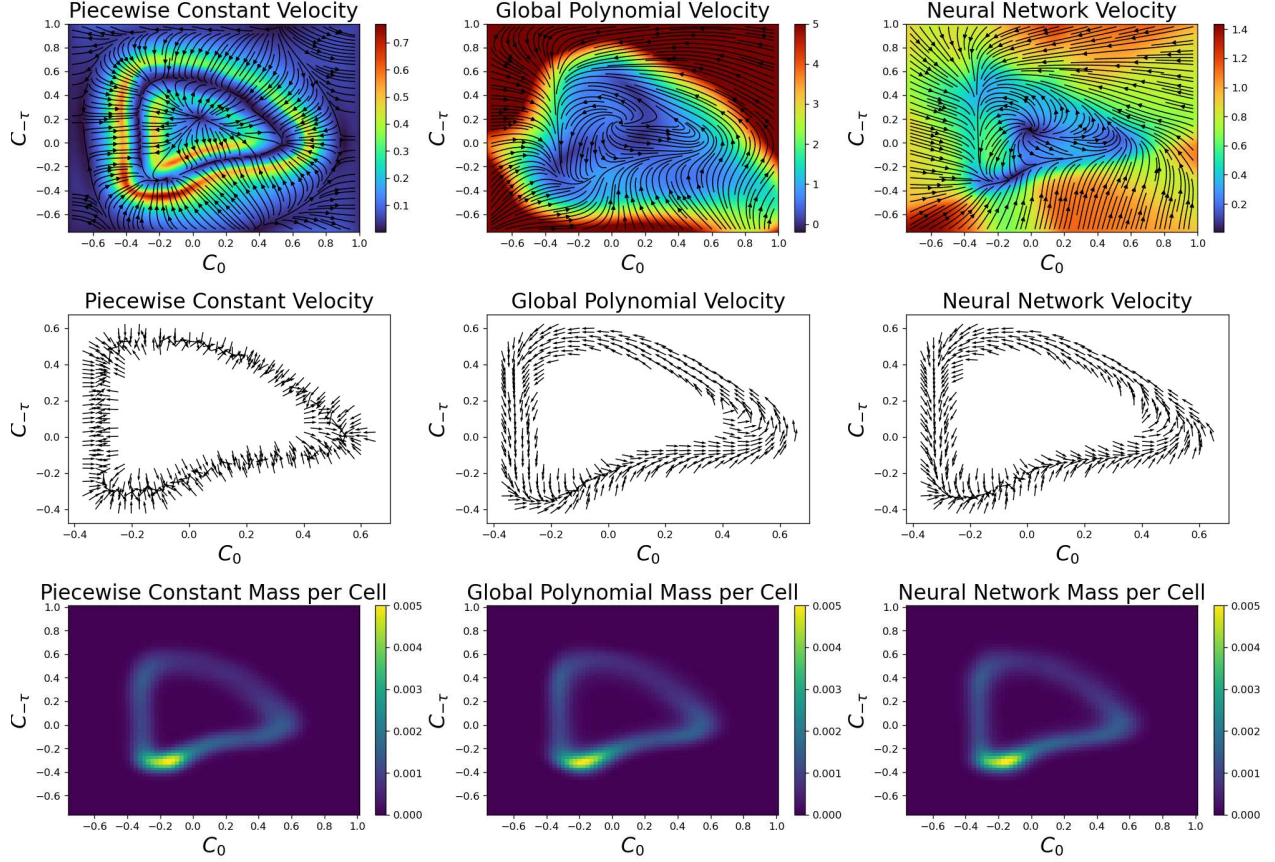


Figure 7: Comparison between the three parameterizations detailed in Section 4.2 for learning a velocity field from the time-delayed Cathode–Pearson signal’s invariant measure, using a diffusion coefficient $D = 0.01$. The learned velocities and densities for the piecewise constant (PC), global polynomial (GP), and neural network (NN) discretizations are shown in the three columns, respectively. We show the velocity field on the full state space (top row), a close-up of the velocity field’s direction near the attracting limit cycle (middle row), and the forward model output $\rho_\varepsilon(v(\theta))$ for each parameterization (bottom row). The resulting parameter spaces of these discretizations have dimensionality of 9800 (PC), 56 (GP), and 400 (NN). The L^2 loss is reduced below .1% of its initial cost for the PC and NN discretizations and reduced below .7% of its initial value for the GP case when we stopped the optimization.

and Lagrangian dynamics and cannot reconstruct zero-diffusion trajectories which form a stable limit cycle. On the other hand, the velocities parameterized by the global polynomial and the neural network are both C^∞ . The differences among these three can clearly be seen via the zoomed-in velocity plots in the second row of Figure 7. The global polynomial and neural network discretizations are both global parameterizations of the velocity, and as such, their values near the domain’s boundary are dictated by the available data in the center of the domain. This causes the polynomial velocity to rapidly increase near the boundary, and a similar effect can also be seen for the neural network.

It is worth noting that the initial condition for the optimization in Figure 7 can play a large role in the reconstructed velocity, which is related to the optimization landscape of the nonconvex optimization problem (2) we tackle. In the case of the piecewise-constant discretization, we initialize all velocities to be significantly less than the diffusion coefficient $D = 0.1$. Thus, diffusion initially dominates in the finite volume solver, and all non-boundary cells will contain nonzero mass, which allows for accurate gradient updates everywhere. This phenomenon can also help neural network training, though it is not always necessary due to the global nature of parameterization. Moreover, we initialize our polynomial basis to form the velocity $(\dot{x}, \dot{y}) = (-y + x(0.1 - x^2 - y^2), x + y(0.1 - x^2 - y^2))$, which describes a globally attracting limit cycle. Thus, to converge to the ground truth limit cycle of the time-delayed Cathode–Pearson signal, this initial velocity only needs to be translated and deformed.

5.3 Temperature Uncertainty Quantification

We now study 2D time-delay embedded data of weekly rolling averages of the temperature in Ithaca, NY, between 2006 and 2020 [11]. We view temperature fluctuations over short time scales as an intrinsic diffusion process and the approximately periodic oscillation of seasonal temperatures driven by some nonzero velocity. Thus, we model the 2D data in delay coordinates as a diffuse limit cycle. We again follow the procedure in Section 5.2.1 to learn a velocity $v(\mathbf{x}; \theta)$ and diffusion coefficient D , which closely matches the occupation measure.

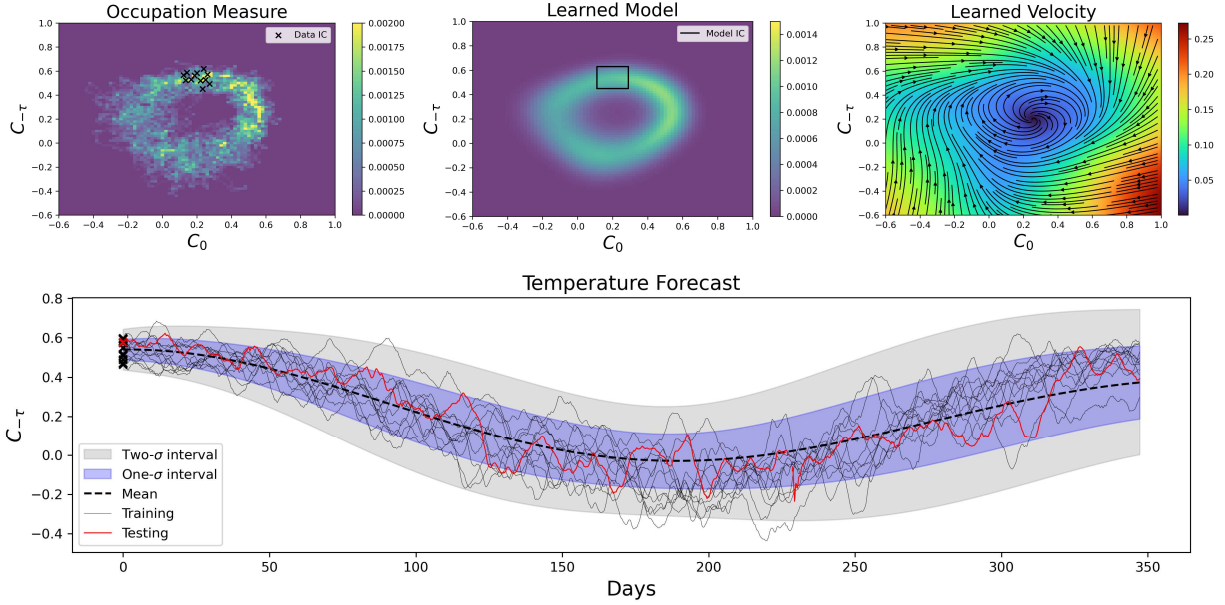


Figure 8: Performing prediction and uncertainty quantification for Ithaca, NY’s temperature in 2019. The top left plot shows the ground truth occupation measure accumulated from 13 years of weekly rolling averaged temperature observations, normalized by an affine transformation to $[-1, 1]$. The top middle and right plots show the learned model and velocity vector field, obtained using the three-step procedure in Section 5.2.1. In the bottom plot, the PDE model with a uniform initialization in the box from the top middle plot is evolved in time and used to quantify the uncertainty in the measurements of C_0 . Observed trajectories of the temperature in delay coordinates with initial conditions displayed in the top left plot are also shown to demonstrate the effectiveness of the learned model. A time delay of $\tau = 280$ days is used, and the model is trained using a neural network parameterization and the KL-divergence objective function.

As in Section 5.2 we can use the trained model $v(\mathbf{x}; \theta)$ to quantify measurement uncertainties through the Fokker–Planck equation (9), whose solution is a probability density in the time-delay coordinates $(C_0, C_{-\tau})$. Specifically, if we know some initial probability distribution that captures the current state of the temperature system well, we can consider the time-evolution of the distribution using our trained model to quantify the uncertainty of future temperature measurements. The process of evolving both the Fokker–Planck PDE from a uniform distribution and the ground truth sample paths from past temperature measurements is shown in Figure 8. The uncertainty bounds from the model accurately capture fluctuations in the training data used to form the occupation measure (plotted in black), as well as a testing sample path previously unseen by the model (plotted in red).

It is also worth noting that the confidence intervals we construct may be larger than the actual range due to several factors, including additional extrinsic noise from filtering the data, modeling errors accumulated from the hypothesis space, numerical diffusion in the forward model, and a sub-optimal embedding dimension. Reducing such errors may result in tighter confidence intervals. Considering time-delays in higher dimensions could yield better predictions of the temperature’s transient behaviors.

5.4 Lorenz-63 System

We conclude this section by studying the Lorenz-63 system [39], defined by

$$\begin{cases} \dot{x} &= c_1(y - x) \\ \dot{y} &= x(c_2 - z) - y, \\ \dot{z} &= xy - c_3z \end{cases} \quad (21)$$

where we consider $(c_1, c_2, c_3) = (10, 28, 8/3)$. For these choices of parameters, the Lorenz-63 system exhibits chaotic behavior and admits a unique physical measure [60]. In Figure 9, we assume that the quantities \dot{y} and \dot{z} are known, and we learn a model for the velocity in the x -direction, using the stochastically-forced Lorenz-63 system’s occupation measure. We emphasize that the samples used to form the occupation measure are not correlated in time and were, in fact, randomly sampled from a trajectory as in [65, Figure 6]. This demonstrates the applicability of the proposed approach for learning the dynamics of physical processes for which measurement times are unknown. From the occupation measure of these samples, we invert the first component \dot{x} of the Lorenz-63 system’s velocity via a neural network parameterization and successfully simulate dynamical trajectories which recover the original Lorenz attractor.

We remark that when \dot{x} , \dot{y} , and \dot{z} are all simultaneously inverted, the optimization is unsuccessful at reconstructing the true velocity (21). While we may be able to learn a velocity that approximately recovers the stationary state of the Lorenz-63 system in the sense of (9), the corresponding dynamical trajectories do not form a chaotic attractor, i.e., the physical property (3) does not hold. Whether the difficulties of inverting all velocity components of the Lorenz-63 system are due to inherent non-uniqueness in the inverse problem or simply inconvenient local minima during training is worth further investigation in future work.

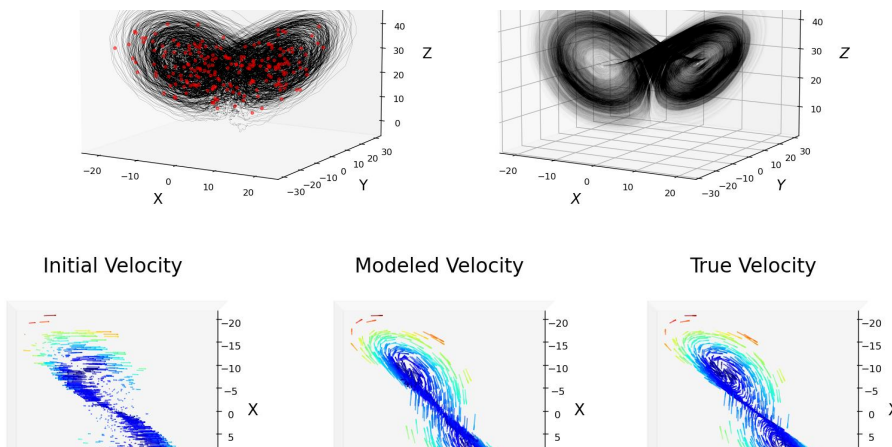


Figure 9: Neural network parameterization of \dot{x} using the Lorenz system’s stochastically perturbed invariant measure with $D = 10$ and $\Delta x = 2$. The top row displays the learned velocity and a single trajectory plotted both with and without diffusion. The bottom row displays the true velocity and true trajectories both with and without diffusion. For visualization of the occupation measure used to learn the model displayed in the top row, we refer to [65].

6 Conclusion

In this paper, we performed large-scale parameter identification to model the velocity $v(\mathbf{x}; \theta)$ of intrinsically noisy autonomous dynamical systems. We first adapted the invariant measure surrogate model $\rho_\varepsilon(v(\theta))$ in [65] based upon the continuity equation to the Fokker–Planck equation. This increased our modeling capacity and prevented overfitting the reconstructed velocity $v(\theta)$ while modeling intrinsically noisy trajectories. We next extended the three-coefficient learning performed in [65] to thousands of coefficients by modeling the velocity $v(\mathbf{x}; \theta)$ via global polynomials, piecewise polynomials, and fully connected neural networks. The efficient gradient computation presented in Section 4 made these large-scale parameterizations of the velocity computationally tractable. We finally studied velocity inversion for invariant measures of time-delay embedded observables. The method of time-delay embedding is useful for analyzing real-world data, where in many cases, only limited observations of complex systems are available. As such, we proceeded to learn the velocity in time-delay coordinates for a Hall-effect thruster system and weekly temperature measurements. Both systems exhibit periodic behavior with intrinsic noise, which led us to model the time-delayed

dynamics as globally attracting limit cycles. Using these models, we predicted future states of the systems and quantified uncertainty in forecasts by evolving the Fokker–Planck equation forward in time, similar to [3].

In future work, there are several computational directions to explore. The first-order upwind finite volume discretization incurs numerical diffusion for large values of Δx and is costly to implement as a forward model for small values of Δx . Higher-order methods would be both more accurate and efficient. Moreover, most globally attracting systems admit invariant measures which are singular with respect to the Lebesgue measure, and consequently, most of the cells in the finite-volume discretization are unused, even if intrinsic noise is present. Therefore, it would be more efficient to solve the Fokker–Planck equation on an unstructured mesh that adapts to the density of the available data.

Given the complex interactions of a large number of variables in real-world systems, the low-dimensional embedding presented in Section 5 may not be sufficient to resolve the full dynamics of the HET and temperature systems. In many cases, time-delay embeddings of dimensionality greater than three are required, and as such, it would be useful to adapt the proposed approach to higher dimensions. The current framework suffers from the curse of dimensionality, so further investigation into mesh-free approaches for approximating invariant measures and solving the resulting PDE-constrained optimization (2) would be fruitful. Finally, the forward model $\rho_\varepsilon(v(\theta))$ should be adapted so that it can describe the invariant measures of multiple attractors.

On the theoretical side, numerous questions about the well-posedness of the inverse problem remain open. Perhaps the most important ones are the following questions, which are directly related to the uniqueness of the reconstructed velocity $v(\mathbf{x}; \theta)$. *Given a physical measure μ of the autonomous dynamics $\dot{\mathbf{x}} = v(\mathbf{x})$, when does there exist another dynamical process $\dot{\mathbf{y}} = w(\mathbf{y})$ which admits the same physical measure μ but satisfies $v(\mathbf{x}) \neq w(\mathbf{x})$ on $\text{supp}(\mu)$? Does the presence of intrinsic noise affect the answer to this question? If the velocity $v(\mathbf{x})$ is not unique on $\text{supp}(\mu)$, is there a restriction to a reasonable function space where uniqueness can be obtained?* A deeper investigation into the stability of the inverse problem is also needed. Specifically, it is desirable to understand how perturbations to a velocity $v(\theta)$ affect the associated physical measure and our surrogate approximation via the upwind finite volume method. Finally, if the uniqueness of the velocity can be guaranteed on $\text{supp}(\mu)$, then the stability of the reconstructed velocity $v(\mathbf{x}; \theta)$ with respect to perturbations of the inference data μ would be the next interesting question.

Acknowledgements

J. Botvinick-Greenhouse was supported by the Department of Defense (DoD) through the National Defense Science & Engineering Graduate (NDSEG) Fellowship Program. R. Martin was partially supported by AFOSR Grants FA9550-20RQCOR098 (PO: Leve) and FA9550-20RQCOR100 (PO: Fahroo). This work was done in part while Y. Yang was visiting the Simons Institute for the Theory of Computing in Fall 2021. Y. Yang acknowledges support from Dr. Max Rössler, the Walter Haefner Foundation and the ETH Zürich Foundation. This material is based upon work supported by the National Science Foundation under Award Number DMS-1913129.

We thank Dr. Chen Li for his helpful suggestions and generosity in sharing code for the approach of Section 4.2.3.

References

- [1] Altan Allawala and J. B. Marston. Statistics of the stochastically forced Lorenz attractor by the Fokker-Planck equation and cumulant expansions. *Physical Review E*, 94(5), nov 2016.
- [2] Ellen Baake, Michael Baake, HG Bock, and KM Briggs. Fitting ordinary differential equations to chaotic data. *Physical Review A*, 45(8):5524, 1992.
- [3] Thomas R Bewley and Atul S Sharma. Efficient grid-based bayesian estimation of nonlinear low-dimensional systems with sparse non-gaussian pdfs. *Automatica*, 48(7):1286–1290, 2012.
- [4] Alex Blumenthal and Lai-Sang Young. Equivalence of physical and SRB measures in random dynamical systems. *Nonlinearity*, 32(4):1494–1524, mar 2019.
- [5] Steven L. Brunton, Bingni W. Brunton, Joshua L. Proctor, Eurika Kaiser, and J. Nathan Kutz. Chaos as an intermittently forced linear system. *Nature Communications*, 8:19, May 2017.
- [6] Steven L Brunton, Joshua L Proctor, and J Nathan Kutz. Discovering governing equations from data by sparse identification of nonlinear dynamical systems. *Proceedings of the National Academy of Sciences*, 113(15):3932–3937, 2016.
- [7] David Chelidze. Reliable Estimation of Minimum Embedding Dimension Through Statistical Analysis of Nearest Neighbors. *Journal of Computational and Nonlinear Dynamics*, 12(5), 07 2017. 051024.

- [8] Ricky TQ Chen, Yulia Rubanova, Jesse Bettencourt, and David K Duvenaud. Neural ordinary differential equations. *Advances in Neural Information Processing Systems*, 31, 2018.
- [9] William Cowieson and Lai-Sang Young. SRB measures as zero-noise limits. *Ergodic Theory and Dynamical Systems*, 25(4):1115–1138, 2005.
- [10] Michael Dellnitz, Gary Froyland, and Oliver Junge. The algorithms behind gaio — set oriented numerical methods for dynamical systems. In Bernold Fiedler, editor, *Ergodic Theory, Analysis, and Efficient Simulation of Dynamical Systems*, pages 145–174, Berlin, Heidelberg, 2001. Springer Berlin Heidelberg.
- [11] Howard J. Diamond, Thomas R. Karl, Michael A. Palecki, C. Bruce Baker, Jesse E. Bell, Ronald D. Leeper, David R. Easterling, Jay H. Lawrimore, Tilden P. Meyers, Michael R. Helfert, Grant Goodge, and Peter W. Thorne. U.S. Climate Reference Network after One Decade of Operations: Status and Assessment. *Bulletin of the American Meteorological Society*, 94(4):485 – 498, 2013.
- [12] Matthew M Dunlop and Yunan Yang. Stability of gibbs posteriors from the wasserstein loss for bayesian full waveform inversion. *SIAM/ASA Journal on Uncertainty Quantification*, 9(4):1499–1526, 2021.
- [13] Daniel Eckhardt, Justin Koo, Robert Martin, Michael Holmes, and Kentaro Hara. Spatiotemporal data fusion and manifold reconstruction in hall thrusters. *Plasma Sources Science and Technology*, 28(4):045005, 2019.
- [14] Manfred Einsiedler and Thomas Ward. *Ergodic Theory: with a view towards Number Theory*. Springer London, London, 2011.
- [15] Björn Engquist, Kui Ren, and Yunan Yang. The quadratic Wasserstein metric for inverse data matching. *Inverse Problems*, 36(5):055001, 2020.
- [16] Björn Engquist and Yunan Yang. Optimal transport based seismic inversion: Beyond cycle skipping. *Communications on Pure and Applied Mathematics*, 2020.
- [17] Urban Fasel, J Nathan Kutz, Bingni W Brunton, and Steven L Brunton. Ensemble-SINDy: Robust sparse model discovery in the low-data, high-noise limit, with active learning and control. *Proceedings of the Royal Society A*, 478(2260):20210904, 2022.
- [18] Colin Fox, Li-Jen Hsiao, and Jeong-Eun Lee. Solutions of the multivariate inverse Frobenius–Perron problem. *Entropy*, 23(7):838, 2021.
- [19] Gary Froyland. *Estimating physical invariant measures and space averages of dynamical systems indicators*. PhD thesis, The University of Western Australia, 1996.
- [20] David F Gleich. Pagerank beyond the web. *SIAM Review*, 57(3):321–363, 2015.
- [21] CM Greve, K Hara, RS Martin, DQ Eckhardt, and JW Koo. A data-driven approach to model calibration for nonlinear dynamical systems. *Journal of Applied physics*, 125(24):244901, 2019.
- [22] S Grossmann and S Thomae. Invariant distributions and stationary correlation functions of one-dimensional discrete processes. *Zeitschrift Naturforschung Teil A*, 32(12):1353–1363, 1977.
- [23] J. Guckenheimer. Dynamics of the Van der Pol equation. *IEEE Transactions on Circuits and Systems*, 27(11):983–989, 1980.
- [24] Jialin Hong and Xu Wang. Invariant measures for stochastic differential equations. In *Invariant Measures for Stochastic Nonlinear Schrödinger Equations*, pages 31–61. Springer, 2019.
- [25] Kurt Hornik, Maxwell Stinchcombe, and Halbert White. Multilayer feedforward networks are universal approximators. *Neural Networks*, 2(5):359–366, 1989.
- [26] Jingwei Hu and Xiangxiong Zhang. Positivity-preserving and energy-dissipative finite difference schemes for the Fokker–Planck and Keller–Segel equations. *IMA Journal of Numerical Analysis*, 05 2022. drac014.
- [27] Wen Huang, Min Ji, Zhenxin Liu, and Yingfei Yi. Steady states of Fokker–Planck equations: I. existence. *Journal of Dynamics and Differential Equations*, 27(3):721–742, 2015.
- [28] Matt Jacobs and Flavien Léger. A fast approach to optimal transport: The back-and-forth method. *Numerische Mathematik*, 146(3):513–544, 2020.
- [29] Junteng Jia and Austin R Benson. Neural jump stochastic differential equations. *Advances in Neural Information Processing Systems*, 32, 2019.
- [30] Anatole Katok and Boris Hasselblatt. *Introduction to the Modern Theory of Dynamical Systems*. Encyclopedia of Mathematics and its Applications. Cambridge University Press, 1995.
- [31] Diederik P. Kingma and Jimmy Ba. Adam: A method for stochastic optimization. In *ICLR (Poster)*, 2015.

- [32] Aaron Kirtland, Jonah Botvinick-Greenhouse, Marianne DeBrito, Megan Osborne, Casey Johnson, Robert S Martin, Samuel J Araki, and Daniel Q Eckhardt. An unstructured mesh approach to nonlinear noise reduction for coupled systems. *arXiv preprint arXiv:2209.05944*, 2022.
- [33] Stefan Klus, Peter Koltai, and Christof Schütte. On the numerical approximation of the Perron-Frobenius and Koopman operator. *Journal of Computational Dynamics*, 3(1):51–77, 2016.
- [34] Andrzej Lasota and Michael C Mackey. *Chaos, fractals, and noise: stochastic aspects of dynamics*, volume 97. Springer Science & Business Media, 1998.
- [35] Yann LeCun, Bernhard Boser, John S Denker, Donnie Henderson, Richard E Howard, Wayne Hubbard, and Lawrence D Jackel. Backpropagation applied to handwritten zip code recognition. *Neural Computation*, 1(4):541–551, 1989.
- [36] Randall J LeVeque et al. *Finite volume methods for hyperbolic problems*, volume 31. Cambridge University Press, 2002.
- [37] Chen Li, Matthew Dunlop, and Georg Stadler. Bayesian neural network priors for edge-preserving inversion. *arXiv preprint arXiv:2112.10663*, 2021.
- [38] Fei Lu, Mauro Maggioni, and Sui Tang. Learning interaction kernels in stochastic systems of interacting particles from multiple trajectories. *Foundations of Computational Mathematics*, pages 1–55, 2021.
- [39] Stefano Luzzatto, Ian Melbourne, and Frederic Paccaut. The Lorenz attractor is mixing. *Communications in Mathematical Physics*, 260(2):393–401, 2005.
- [40] H.G. Ma and C.Z. Han. Selection of embedding dimension and delay time in phase space reconstruction. *Frontiers of Electrical and Electronic Engineering in China*, 1:111–114, 2006.
- [41] N. A. MacDonald, M. A. Cappelli, and W. A. Hargus Jr. Time-Synchronized Continuous Wave Laser-Induced Fluorescence on an Oscillatory Xenon Discharge. *Review of Scientific Instruments*, 83(113506):1–8, 2012.
- [42] Adam Maus and Julien Clinton Sprott. Neural network method for determining embedding dimension of a time series. *Communications in Nonlinear Science and Numerical Simulation*, 16, 05 2010.
- [43] Ricardo Mañé. *Ergodic Theory and Differentiable Dynamics*. Springer Berlin, Heidelberg, 1987.
- [44] Andre M McDonald and Michaël A van Wyk. A novel approach to solving the generalized inverse Frobenius–Perron problem. In *2020 IEEE International Symposium on Circuits and Systems (ISCAS)*, pages 1–5. IEEE, 2020.
- [45] André M. McDonald, Michaël A. van Wyk, and Guanrong Chen. The inverse Frobenius–Perron problem: A survey of solutions to the original problem formulation. *AIMS Mathematics*, 6(10):11200–11232, 2021.
- [46] Claas Michalik, Ralf Hannemann, and Wolfgang Marquardt. Incremental single shooting—a robust method for the estimation of parameters in dynamical systems. *Computers & Chemical Engineering*, 33(7):1298–1305, 2009.
- [47] Francisco J Montáns, Francisco Chinesta, Rafael Gómez-Bombarelli, and J Nathan Kutz. Data-driven modeling and learning in science and engineering. *Comptes Rendus Mécanique*, 347(11):845–855, 2019.
- [48] Calvin C Moore. Ergodic theorem, ergodic theory, and statistical mechanics. *Proceedings of the National Academy of Sciences*, 112(7):1907–1911, 2015.
- [49] Elisa Negrini, Giovanna Citti, and Luca Capogna. System identification through lipschitz regularized deep neural networks. *Journal of Computational Physics*, 444:110549, 2021.
- [50] Xiaokai Nie and Daniel Coca. A matrix-based approach to solving the inverse frobenius–perron problem using sequences of density functions of stochastically perturbed dynamical systems. *Communications in Nonlinear Science and Numerical Simulation*, 54:248–266, 2018.
- [51] Xiaokai Nie, Daniel Coca, Jingjing Luo, and Mark Birkin. Solving the inverse Frobenius–Perron problem using stationary densities of dynamical systems with input perturbations. *Communications in Nonlinear Science and Numerical Simulation*, 90:105302, 2020.
- [52] Levon Nurbekyan, Wanzhou Lei, and Yunan Yang. Efficient natural gradient descent methods for large-scale optimization problems. *arXiv preprint arXiv:2202.06236*, 2022.
- [53] Grigorios A. Pavliotis. *Stochastic Processes and Applications*. Springer New York, NY, 2014.
- [54] D. Pingel, Peter Schmelcher, and F. Diakonou. Theory and examples of the inverse Frobenius–Perron problem for complete chaotic maps. *Chaos (Woodbury, N.Y.)*, 9:357–366, 07 1999.
- [55] P. Ramachandran and G. Varoquaux. Mayavi: 3D Visualization of Scientific Data. *Computing in Science & Engineering*, 13(2):40–51, 2011.

- [56] Tim Sauer, James A. Yorke, and Martin Casdagli. Embedology. *Journal of Statistical Physics*, 65(3):579–616, Nov 1991.
- [57] Thibault Séjourné, François-Xavier Vialard, and Gabriel Peyré. Faster unbalanced optimal transport: Translation invariant sinkhorn and 1-d frank-wolfe. In *International Conference on Artificial Intelligence and Statistics*, pages 4995–5021. PMLR, 2022.
- [58] George Sugihara, Robert May, Hao Ye, Chih hao Hsieh, Ethan Deyle, Michael Fogarty, and Stephan Munch. Detecting causality in complex ecosystems. *Science*, 338(6106):496–500, 2012.
- [59] Floris Takens. Detecting strange attractors in turbulence. In *Dynamical Systems and Turbulence, Warwick 1980*, pages 366–381. Springer, 1981.
- [60] Warwick Tucker. The Lorenz attractor exists. *Comptes Rendus de l’Académie des Sciences - Series I - Mathematics*, 328(12):1197–1202, 1999.
- [61] Cédric Villani. *Topics in optimal transportation*, volume 58. American Mathematical Soc., 2021.
- [62] Sebastian Wallot and Dan Mønster. Calculation of average mutual information (AMI) and false-nearest neighbors (FNN) for the estimation of embedding parameters of multidimensional time series in Matlab. *Frontiers in psychology*, 9:1679, 2018.
- [63] Hua Wei, Chacha Chen, Chang Liu, Guanjie Zheng, and Zhenhui Li. Learning to simulate on sparse trajectory data. In *Joint European Conference on Machine Learning and Knowledge Discovery in Databases*, pages 530–545. Springer, 2020.
- [64] Nijun Wei. Solutions of the inverse Frobenius–Perron problem. Master’s thesis, Concordia University, July 2015. Unpublished.
- [65] Yunan Yang, Levon Nurbekyan, Elisa Negrini, Robert Martin, and Mirjeta Pasha. Optimal transport for parameter identification of chaotic dynamics via invariant measures. *arXiv preprint arXiv:2104.15138*, 2021.
- [66] Lai-Sang Young. What are SRB measures, and which dynamical systems have them? *Journal of statistical physics*, 108(5):733–754, 2002.